Monthly Notices of the ROYAL ASTRONOMICAL SOCIETY

MNRAS **535,** 2724–2741 (2024) https://doi.org/10.1093/mnras/stae2538
Advance Access publication 2024 November 12

The impact of periastron passage on the X-ray and optical properties of the Symbiotic System R Aquarii

D. A. Vasquez-Torres [1]★ J. A. Toalá [1]† A. Sacchi [2] M. A. Guerrero [3] E. Tejeda [4] M. Karovska [2] and R. Montez Jr [2]

[1]*Instituto de Radioastronomía y Astrofísica, Universidad Nacional Autónoma de México, 58090 Morelia, Michoacán, Mexico*
[2]*Center for Astrophysics | Harvard & Smithsonian, 60 Garden Street, Cambridge, MA 02138, USA*
[3]*Instituto de Astrofísica de Andalucía, IAA–CSIC, Glorieta de la Astronomía S/N, E-18008 Granada, Spain*
[4]*CONAHCYT – Instituto de Física y Matemáticas, Universidad Michoacana de San Nicolás de Hidalgo, Ciudad Universitaria, 58040 Morelia, Mich., Mexico*

Accepted 2024 November 7. Received 2024 November 4; in original form 2024 September 30

ABSTRACT

Multi-epoch *Chandra* and *XMM–Newton* observations of the symbiotic system R Aquarii (R Aqr) spanning 22 yr are analysed by means of a reflection model produced by an accretion disc. This methodology helps dissecting the contribution from different components in the X-ray spectra of R Aqr: the soft emission from the jet and extended emission, the heavily extinguished plasma component of the boundary layer and the reflection contribution, which naturally includes the 6.4 keV Fe fluorescent line. The evolution with time of the different components is studied for epochs between September 2000 and December 2022, and it is found that the fluxes of the boundary layer and that of the reflecting component increase as the stellar components in R Aqr approach periastron passage, a similar behaviour is exhibited by the shocked plasma produced by the precessing jet. Using publicly available optical and UV data we are able to study the evolution of the mass-accretion rate $\dot{M}_{\rm acc}$ and the wind accretion efficiency η during periastron. These exhibit a small degree of variability with median values of $\dot{M}_{\rm acc}$=7.3×10^{-10} M$_\odot$ yr^{-1} and η=7×10^{-3}. We compare our estimations with predictions from a modified Bondi–Hoyle–Lyttleton accretion scenario.

Key words: accretion, accretion discs – binaries: symbiotic – ISM: individual objects: R Aquarii – ISM: jets and outflows – X-rays: binaries – X-rays: stars.

1 INTRODUCTION

R Aquarii (hereinafter R Aqr) is one of the closest symbiotic systems, with an estimated distance d ranging from about ∼180 to ∼260 pc (Liimets et al. 2018; Alcolea et al. 2023), with the farthest value of 387^{+50}_{-110} pc estimated from *Gaia* parallax measurements (Bailer-Jones et al. 2021). Its proximity allows astronomers to characterize the symbiotic system and its associated nebula with extreme detail. For decades, optical studies have shown the intricate morphology of the nebula around R Aqr (see Liimets et al. 2018, and references therein) consisting of (at least) three main structures: an outer hourglass structure encompassing an inner bipolar structure and a spiral-like filament entwined around the latter. It has been argued recently by Santamaría et al. (2024) that the action of the precessing jet at the core of R Aqr is responsible for the current morphology of the nebula associated with this symbiotic system.

The most recent orbit calculations of this symbiotic system predict an orbital period of 42.4 ± 0.2 yr (see e.g. Alcolea et al. 2023), an eccentricity of 0.45 ± 0.01, an inclination of the orbital plane with respect to the line of sight of 110.7 ±1.0°, and a measured semimajor axis of about 47–57 mas (Bujarrabal et al. 2018; Alcolea et al. 2023). The periastron is estimated to have occurred during 2019.9 ± 0.1. R Aqr consists of a white dwarf (WD) with a mass of $M_{\rm WD}$ = 0.7 ± 0.2 M$_\odot$ and a M-type cool component with a mass of 1.0 ± 0.2 M$_\odot$. The cool component is a long-period Mira-type variable with a pulsation period of P = 388.1 ± 0.1 d (Gromadzki & Mikołajewska 2009). These parameters translate into a radius for the M-type star of ∼250 R$_\odot$ using the period–mass relationship (see Vassiliadis & Wood 1993).

Several authors have estimated the mass accretion rate ($\dot{M}_{\rm acc}$) of the WD component using a variety of methodologies and assumptions, with values in the ∼ 10^{-9}–10^{-8} M$_\odot$ yr^{-1} range (see e.g. Burgarella, Vogel & Paresce 1992; Henney & Dyson 1992; Ragland et al. 2008; Melnikov, Stute & Eislöffel 2018; Sacchi et al. 2024). Burgarella et al. (1992) argued against the presence of an accretion disc around the WD component in R Aqr and the lack of flickering in the optical spectra of this symbiotic system seems to be in line with that result (Snaid et al. 2018). However, based on near-infrared (IR) observations, Hinkle et al. (2022) suggested that an accretion disc is present and has a size of $\gtrsim$5 au, with estimations of 4 au during periastron passage given the elliptical orbit.

The first detection of X-ray emission from R Aqr was made with the *Einstein Observatory* in 1979 (Jura & Helfand 1984), followed by observations from *European X-ray Observatory Satellite EXOSAT* (*EXOSAT*, Viotti et al. 1987) and *Röntgensatellit* (*ROSAT*, Hunsch et al. 1998).However, it was not until the advent of *Chandra*

★ E-mail: d.vasquez@irya.unam.mx
† Visiting astronomer at the IAA–CSIC as part of the Centro de Excelencia Severo Ochoa Visiting-Incoming programme.

Table 1. Details of the X-ray observations of R Aqr analysed in this paper.

Instrument	Obs. ID.	Observation date (UTC)	Epoch (yr)	Exp. time (ks)	Useful time (ks)	Net count rate (cnt ks^{-1})
Chandra ACIS-S	651	2000-09-10T04:58:36	2000.69	22.72	22.72	5.8±0.5
Chandra ACIS-S	4546	2003-12-31T15:04:37	2003.99	36.52	36.13	6.4±0.4
Chandra ACIS-S	5438	2005-10-09T19:08:50	2005.78	66.76	66.76	8.9±0.4
Chandra ACIS-S	19015	2017-10-13T13:48:02	2017.79	75.66	75.46	34.5±0.7
Chandra ACIS-S	20809	2017-10-11T08:22:21	2017.78	49.37	48.19	29.9±0.8
Chandra ACIS-S	23108	2020-01-11T23:53:56	2020.03	47.48	46.63	42.3±1.0
Chandra ACIS-S	23325	2021-04-29T21:38:04	2021.33	31.91	30.94	32.8±1.0
Chandra ACIS-S	24341	2021-04-30T18:00:36	2021.34	35.60	35.21	26.6±0.8
Chandra ACIS-S	27322	2022-10-03T18:33:27	2022.75	18.83	18.73	10.9±0.8
Chandra ACIS-S	27333	2022-09-26T11:53:07	2022.74	27.21	26.78	16.8±0.8
Chandra ACIS-S	27467	2022-10-04T06:14:58	2022.76	19.81	19.62	14.9±0.9
Chandra ACIS-S	27468	2022-10-09T17:27:37	2022.78	14.88	14.58	18.0±1.1
XMM–Newton EPIC-pn	0304050101	2005-06-30T07:21:20	2005.50	70.64	35.75	53.3±1.3

that the extended emission from the jet and that from the central engine were finally resolved (Kellogg, Pedelty & Lyon 2001). These authors showed that the spectrum of the central source of R Aqr was described by a combination of soft X-ray emission (E <2.0 keV) and a contribution at higher energies with a peak at 6.4 keV attributed to the Fe Kα fluorescent line. This type of X-ray spectra from symbiotic systems is classified as a β/δ-type (Luna et al. 2013). In combination with subsequent *Chandra* observations obtained by the end of year 2003, Kellogg et al. (2007) demonstrated that the X-ray spectra of the jets from R Aqr were best fit by plasma temperatures of ∼0.12–0.15 keV ($\approx 1.5 \times 10^6$ K), very likely the result of an adiabatic shock produced by the jet velocity of a few times 10^2 km s^{-1}. More recently, Toalá et al. (2022) presented the analysis of archival *XMM–Newton* observations obtained during 2005 and discovered the presence of extended supersoft X-ray emission ($kT \approx 0.09$ keV). This supersoft emission fills the large-scale structures observed by nebular images of R Aqr and it is present even when modelling the emission from the X-ray-emitting clumps from the jets. Toalá et al. (2022) suggested that the origin of the extended supersoft X-ray emission is material produced by the ongoing fast jets that has expanded and cooled down.

Chandra observations since 2017 were carried out as part of a multimission, multiwavelength campaign to study the evolution of R Aqr during periastron passage (PI: M. Karovska; e.g. Huang et al. 2023; Sacchi et al. 2024). By analysing *Chandra* and *Swift* X-ray observations around the periastron passage, Sacchi et al. (2024) reported an increase in the soft X-ray flux while the hard emission showed a decrease in flux. Several scenarios are proposed to explain this behaviour, focusing on changes in the physical properties or geometry of the surrounding medium, possibly as a result of the periastron passage. Sacchi et al. (2024) adopted Gaussian components to fit the 6.4 keV Fe fluorescent line in addition to power-law models to fit the intermediate 2.0–4.0 keV energy range. Since the X-ray emission from symbiotic systems are expected to have a shock origin (Mukai 2017), a more suitable model is warranted.

In this paper, we present a reanalysis of the available X-ray *Chandra* and *XMM–Newton* observations of R Aqr. We include the effects of reflection physic models developed by our team (e.g. Toalá et al. 2023, 2024; Toalá 2024), which help us dissecting the contributions from the different components of the X-ray spectra. In addition, we also used publicly available optical spectra to produce an unprecedented view of the accretion process in such an iconic symbiotic system such as R Aqr. We note that given the relatively large dispersion in the determination of a distance to R Aqr (see above), we will adopt a somewhat conservative distance value of $d = 200^{+60}_{-20}$ pc, where the error values correspond to the different distance estimated by other authors. Given that parallax distance measurements of symbiotic stars are affected by significant uncertainties due to their extension, colours, and orbital motion, we discount the distance estimated by *Gaia* (Linford et al. 2019; Sion et al. 2019).

This paper is organized as follows. In Section 2, we describe the observations used in this work and their preparation. Section 3 describes the analysis and the results. A discussion is presented in Section 4 and, finally, our summary and conclusions are presented in Section 5.

2 OBSERVATIONS AND DATA PREPARATION

2.1 X-ray data

R Aqr is one of the most observed X-ray-emitting symbiotic systems. It has been observed by most major X-ray observatories. In this work, we present a joint analysis of *Chandra* and *XMM–Newton* observations to study the impact of reflection physics on the estimation of the different spectral components of its X-ray emission. These observations are of particular interest because they cover the last 22 yr of evolution of R Aqr since its apastron in ≃1998.7 and some years after periastron passage in ≃2019.9 (Sacchi et al. 2024).

R Aqr has been observed with the Advanced CCD Imaging Spectrometer (ACIS)-S onboard *Chandra* at 12 different epochs between 2000 and 2022, corresponding to a total observing time of 446.75 ks. All observations were retrieved from the Chandra Data Archive[1] and their details are listed in Table 1. The *Chandra* ACIS-S observations were processed with the Chandra Interactive Analysis of Observations (CIAO, version 4.14; Fruscione et al. 2006).

An event file per epoch was produced by reprocessing the data with the CIAO task `chandra_repro`. After removing periods of high background, the observations did not reduce their net exposure times significantly (see Table 1). The spectra of R Aqr were extracted from a circular aperture with 5 arcsec in radius with the CIAO task `specextract`. The background extraction region was defined by another circular aperture with 15 arcsec in radius in the vicinity of R Aqr with no contribution from this symbiotic system or the extended emission produced by the jets (see Sacchi et al. 2024, and references therein). The CIAO task `specextract` simultaneously

[1] https://cda.harvard.edu/chaser/

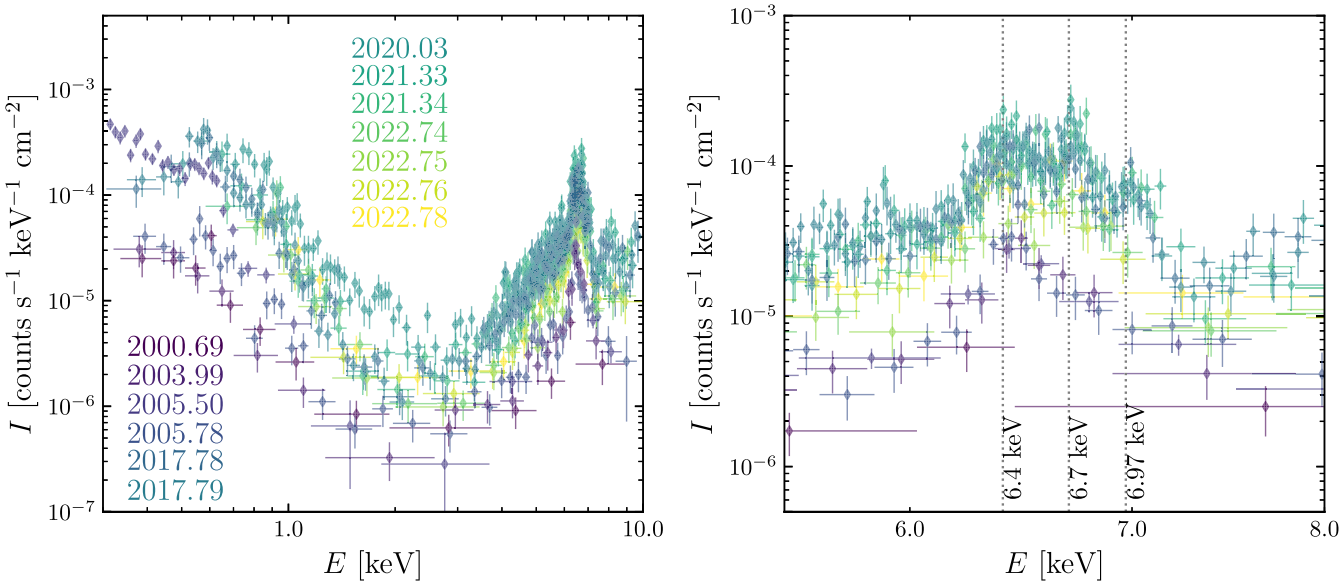

Figure 1. Background-subtracted *Chandra* ACIS-S and *XMM–Newton* EPIC-pn spectra of R Aqr. Different epochs of observation are illustrated and labelled (see Table 1 for details). The right panel shows a zoom into the 5.5–8.0 keV energy range to illustrate the contribution of the 6.4, 6.7, and 6.79 keV Fe emission lines.

produces the redistribution matrix and ancillary response files (RMF and ARF, respectively). All background-subtracted *Chandra* ACIS-S spectra of R Aqr are presented in Fig. 1. The spectra were binned based on a minimum of 10 counts per bin.

R Aqr has been observed once by *XMM–Newton* using the European Photon Imaging Camera (EPIC) on 2005 June 30 (Obs. ID. 0304050101) with a total exposure time of 72.52 ks. The observation data files were retrieved from the XMM-Newton Science Archive[2] and were processed following standard routines with the Science Analysis Software (SAS, version 20.0; Gabriel et al. 2004) with the calibration matrices obtained on 2024 June 28.

The EPIC spectra of R Aqr were extracted from a circular aperture with 1 arcmin in radius using the SAS task `evselect`. The background was defined by a similar aperture but from a region with no contribution from the extended X-ray emission originally reported in Toalá et al. (2022). The corresponding RMF and ARF files were produced with the `rmfgen` and `arfgen` tasks, respectively. Given its superior effective area with respect to the MOS detectors, in this paper we will only concentrate in the analysis of the EPIC-pn spectrum. This is presented in Fig. 1 alongside the *Chandra* ACIS-S spectra of R Aqr. This EPIC pn spectrum is required to have a minimum of 60 counts per bin. The details of the *XMM–Newton* EPIC pn observations are also presented in Table 1.

2.2 Optical data

To complement the X-ray observations, we searched for publicly available contemporary optical data. Optical spectra of R Aqr were retrieved from the ARAS spectral data base[3] (Teyssier 2019), which provides spectra from multiple epochs thanks to its international monitoring programme of symbiotic stars. Only flux-calibrated spectra were retrieved from the ARAS data base. Table 2 lists the details of the individual spectra analysed in this work (observer, observation location, spectral resolution, and wavelength range covered by each spectrum). These include spectra obtained between 2017 October 18 and 2022 December 10.

The flux-calibrated ARAS spectra were inspected in IRAF (Tody 1993) to calculate individual reddening $c(\mathrm{H}\beta)$ values for each spectrum from the Hα/Hβ line ratio. However, we obtained Hα/H$\beta \gtrsim 3$ that might suggest that the recombination Case B might not be applicable to R Aqr. This issue is known for S-type symbiotic systems where the Hα/Hβ ratio has been found to be reddening-free (Mikolajewska & Kenyon 1992; Mikolajewska, Acker & Stenholm 1997). Consequently, we decided to deredden the optical spectra by adopting the hydrogen column density (N_{H}) reported towards the direction of R Aqr. The N_{H} column density tool of HEASARC[4] suggests a value of 1.83×10^{20} cm^{-2}, which adopting $R_{\mathrm{V}} = 3.1$ can be converted into an extinction A_{V} of 0.1.

The spectra were then corrected for extinction using the `remove` module from the `extinction`[5] PYTHON library. The extinction function is calculated using the `ccm89` module from the same library, which is based on the extinction law by Cardelli, Clayton & Mathis (1989). In Fig. 2, we present two examples of flux-calibrated, extinction-corrected ARAS spectra that are contemporaneous with two of the X-ray epochs of observations, while the rest of them are presented in Appendix A.

3 ANALYSIS AND RESULTS

The X-ray spectra presented in Fig. 1 illustrate the X-ray evolution of R Aqr over a time span of 22 yr from October 2000 to September 2022, covering about half of the orbital period of the system. The left panel of Fig. 1 shows noticeable variations in the total apparent X-ray flux of R Aqr in the 0.3–10.0 keV. The earliest observations (2000.69 and 2003.99) have the faintest observed fluxes, while there is a peak

[2] https://www.cosmos.esa.int/web/xmm-newton/xsa
[3] https://aras-database.github.io/database/index.html
[4] https://heasarc.gsfc.nasa.gov/cgi-bin/Tools/w3nh/w3nh.pl
[5] https://extinction.readthedocs.io/en/latest/index.html

Table 2. Details of the optical spectra of R Aqr obtained from the ARAS spectral data base. $F_{\rm opt}$ and $L_{\rm opt}$ are the estimated optical flux and luminosity of the accretion disc, respectively. $\Delta\lambda$ denotes the complete wavelength range of each spectrum, while $\Delta\lambda_{\rm int}$ is the integration range used to estimate the optical flux ($F_{\rm opt}$) of the accretion disc. Here, $\dot{M}_{\rm acc}$ has been computed including $L_{\rm UV}$ and $L_{\rm opt}$.

Observation date (UTC)	JD 2400000 (d)	Observer	Site	R	$\Delta\lambda$ (Å)	$\Delta\lambda_{\rm int}$ (Å)	M-type	$F_{\rm opt}$ (erg cm^{-2} s^{-1})	$L_{\rm opt}$ (L$_\odot$)	$\dot{M}_{\rm acc}$ (M$_\odot$ yr^{-1})
2017-10-18T13:45	58045.073	P. Luckas	SPO-AU	536	3700–7399	3860–6000	M9	3.12×10^{-10}	$0.39^{+0.23}_{-0.08}$	$(1.2^{+0.5}_{-0.3}) \times 10^{-9}$
2019-11-15T10:32	58802.939	T. Bohlsen	ARM-AU	1760	3800–7400	3860–5450	M6	6.26×10^{-11}	$0.08^{+0.05}_{-0.02}$	$(4.5^{+1.9}_{-1.1}) \times 10^{-10}$
2020-01-12T02:02	58860.585	F. Sims	DCO-US	1021	3715–7305	3860–5855	M5	9.45×10^{-11}	$0.12^{+0.07}_{-0.02}$	$(5.4^{+2.1}_{-1.4}) \times 10^{-10}$
2020-01-13T02:11	58861.591	F. Sims	DCO-US	1021	3715–7305	3860–5597	M5	9.03×10^{-11}	$0.11^{+0.07}_{-0.02}$	$(5.3^{+2.0}_{-1.3}) \times 10^{-10}$
2020-01-14T02:12	58862.592	F. Sims	DCO-US	1010	3716–7305	3860–5737	M5	8.87×10^{-11}	$0.11^{+0.07}_{-0.02}$	$(5.2^{+2.0}_{-1.3}) \times 10^{-10}$
2020-01-19T01:59	58867.583	F. Sims	DCO-US	1066	3719–7305	3860–5738	M6	7.22×10^{-11}	$0.09^{+0.05}_{-0.02}$	$(4.8^{+1.8}_{-1.2}) \times 10^{-10}$
2020-07-30T08:51	59060.869	F. Sims	DCO-US	1066	3719–7305	3860–5450	M6	2.76×10^{-11}	$0.35^{+0.21}_{-0.07}$	$(1.1^{+0.4}_{-0.3}) \times 10^{-9}$
2020-10-13T06:43	59135.780	F. Sims	DCO-US	757	3710–7296	3860–6000	M8	1.62×10^{-10}	$0.20^{+0.12}_{-0.04}$	$(7.3^{+2.8}_{-2.0}) \times 10^{-10}$
2020-10-22T05:08	59144.714	F. Sims	DCO-US	1057	3716–7304	3860–5930	M8	1.48×10^{-10}	$0.19^{+0.11}_{-0.04}$	$(6.9^{+2.7}_{-1.8}) \times 10^{-10}$
2020-11-26T03:07	59179.630	F. Sims	DCO-US	1057	3716–7304	3860–5230	M8	1.10×10^{-10}	$0.14^{+0.08}_{-0.03}$	$(5.8^{+2.2}_{-1.5}) \times 10^{-10}$
2021-11-11T02:54	59529.621	F. Sims	DCO-US	1032	3695–7283	3860–5700	M8	1.29×10^{-10}	$0.16^{+0.10}_{-0.03}$	$(6.3^{+2.4}_{-1.7}) \times 10^{-10}$
2022-10-02T06:40	59854.778	F. Sims	DCO-US	1067	3718–7307	3860–6000	M9	4.51×10^{-10}	$0.56^{+0.34}_{-0.11}$	$(1.6^{+0.6}_{-0.5}) \times 10^{-9}$
2022-10-23T05:36	59875.734	F. Sims	DCO-US	1026	3718–7307	3860–6000	M9	3.00×10^{-10}	$0.38^{+0.23}_{-0.07}$	$(1.1^{+0.5}_{-0.3}) \times 10^{-9}$
2022-10-29T05:29	59881.729	F. Sims	DCO-US	1069	3729–7291	3860–6000	M9	2.71×10^{-10}	$0.34^{+0.20}_{-0.07}$	$(1.0^{+0.4}_{-0.3}) \times 10^{-9}$
2022-11-01T04:43	59884.697	F. Sims	DCO-US	1070	3728–7290	3860–6000	M9	2.56×10^{-10}	$0.32^{+0.19}_{-0.06}$	$(1.0^{+0.4}_{-0.3}) \times 10^{-9}$
2022-11-09T03:34	59892.649	F. Sims	DCO-US	1066	3729–7300	3860–6000	M9	2.21×10^{-10}	$0.27^{+0.16}_{-0.06}$	$(9.0^{+3.6}_{-2.5}) \times 10^{-10}$
2022-11-17T03:58	59900.665	F. Sims	DCO-US	1044	3729–730	3860–6000	M9	1.82×10^{-10}	$0.23^{+0.14}_{-0.05}$	$(7.3^{+2.9}_{-2.0}) \times 10^{-10}$
2022-11-20T02:58	59903.624	F. Sims	DCO-US	1084	3729–7300	3860–6000	M9	1.62×10^{-10}	$0.20^{+0.12}_{-0.04}$	$(7.9^{+3.1}_{-2.1}) \times 10^{-10}$
2022-11-25T04:39	59908.694	F. Sims	DCO-US	1048	3730–7301	3860–6000	M9	1.76×10^{-10}	$0.22^{+0.13}_{-0.04}$	$(7.7^{+3.0}_{-2.1}) \times 10^{-10}$
2022-11-30T04:09	59913.673	F. Sims	DCO-US	1048	3727–7300	3860–6000	M9	1.83×10^{-10}	$0.23^{+0.14}_{-0.05}$	$(7.9^{+3.1}_{-2.1}) \times 10^{-10}$
2022-12-10T03:28	59923.645	F. Sims	DCO-US	1055	3730–7301	3860–6000	M9	1.57×10^{-10}	$0.20^{+0.12}_{-0.04}$	$(7.2^{+2.8}_{-1.9}) \times 10^{-10}$

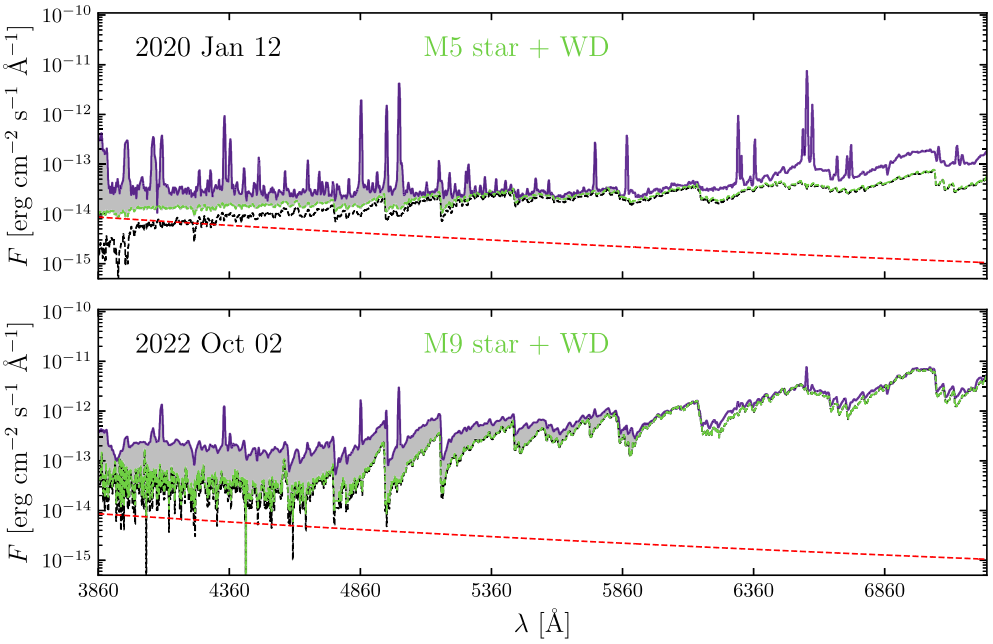

Figure 2. Examples of extinction-corrected, flux-calibrated optical spectra of R Aqr (solid purple lines), obtained from the ARAS Spectral Data base on 2020 January 12 (top) and 2022 October 02 (bottom). The spectra are compared with M-type star models from Fluks et al. (1994) (black dashed lines) and the contribution from the WD with the parameters estimated in Appendix B ($T_{\rm eff}$ = 25, 000 K and L= 0.19 L$_\odot$; red dashed line). A combined spectrum (M-type star + WD) is shown with a (green) dashed line. The grey shaded area represents the contribution of the accretion disc to the optical flux.

over epochs ∼2017–2020, followed by an apparent decrease to the last observation during 2022.

The right panel of Fig. 1 shows the variation of the three Fe emission lines for the 22 yr period studied here. The Fe fluorescent line at 6.4 keV is present in all epochs, thus suggesting that reflection is an unavoidable component. At early epochs, the 5.5–8.0 keV energy range is dominated by the 6.4 keV fluorescent line, with the contribution from the Fe emission lines at 6.7 and 6.97 keV becoming relevant at epochs later than 2005. In fact, the flux in this energy range increases with time suggesting that the flux of the heavily extinguished plasma component associated with the boundary layer increased its flux in the later epochs.

The analysis of the X-ray spectra was performed with the X-Ray Spectral Fitting Package XSPEC (version 12.12.1; Arnaud 1996). Following previous analyses of the X-ray observations of R Aqr (Kellogg et al. 2001, 2007; Sacchi et al. 2024) and other β/δ-type symbiotic stars (e.g. Karovska et al. 2007; Zhekov & Tomov 2019), we adopted two distinct hydrogen column density components ($N_{\rm H1}$ and $N_{\rm H2}$) using the Tuebingen–Boulder ISM absorption model (`tbabs`; Wilms, Allen & McCray 2000) included in XSPEC. $N_{\rm H1}$ is usually found to affect the soft spectral region very likely produced by the extended emission, while the second and larger extinction $N_{\rm H2}$ affects the emission from the boundary layer and the contribution from the reflection component. For the X-ray emission from R Aqr, we adopted an emission spectrum from collisionally ionized diffuse gas, specifically, the `apec` model included in XSPEC.[6] The abundances were set to solar values from Lodders, Palme & Gail (2009).

3.1 The accretion disc as a source of reflection

The ubiquitous presence of the fluorescent Fe emission line at 6.4 keV in the X-ray spectra of R Aqr suggests a more complex and physically meaningful reflection-based analysis of the emission than the often used Gaussian profile. Indeed, reflection from the accretion disc around the WD component in symbiotic systems has been used before to study the impact on the presence of the 6.4 keV Fe emission line (e.g. Ishida et al. 2009; Lopes de Oliveira et al. 2018; Toalá et al. 2023, 2024) and a similar scenario will be adopted here for R Aqr.

Using the best estimates for the stellar components and their orbital parameters, we can approximate the size of the accretion disc. Recent estimates of the semimajor axis of the binary orbit predict $a =$ 47–57 mas (Bujarrabal et al. 2018; Alcolea et al. 2023) which, at a distance of $d = 200^{+60}_{-20}$ pc, translates to a maximum value of $a = 5.5^{+1.7}_{-0.6} \times 10^{-5}$ pc or $a = 11.4^{+3.5}_{-1.1}$ au.

Using the approximation for the effective Roche lobe radius (see Eggleton 1983)

$$\frac{r_{\rm L}}{a} = \frac{0.49q^{2/3}}{0.6q^{2/3} + \ln(1+q^{1/3})}, \quad (1)$$

where q is the companion to the WD mass ratio, we obtain $r_{\rm L} = 4.7^{+1.4}_{-0.5}$ au for a WD mass of $M_{\rm WD} = 0.7$ M$_\odot$ and a mass for the red giant companion of 1.0 M$_\odot$ (following the mass ratio of 1.4 and a total mass of the binary of 1.7 ± 0.1 M$_\odot$ reported in Alcolea et al. 2023). We note that Hinkle et al. (2022) proposed a very similar radius of 5 au for the accretion disc.

We have generated reflection models of disc-like geometries using the SKIRT radiative transfer code (version 9; Camps & Baes 2020) that currently includes the calculations for the radiative transfer of X-ray photons (Vander Meulen et al. 2023). We fixed the geometry of the disc to a flared disc with an opening angle of $\phi = 30°$ and inner and outer radii of $r_{\rm in} = 5.4\times10^{-4}$ au (= 0.012 R$_\odot$)[7] and $r_{\rm out} =$ 5 au, respectively.[8] Several values for the averaged column density of the disc were explored ($N_{\rm H,ref} = 10^{24}$, 5×10^{24}, 10^{25}, 5×10^{25}, and 10^{26} cm^{-2}), but the best quality fits to the X-ray data resulted when using $N_{\rm H,ref} = 5\times10^{24}$ cm^{-2}. Finally, the accretion disc is assumed to be ionized with a temperature of $T = 10^4$ K.

Bujarrabal et al. (2021) presented numerical simulations of the interaction of a WD accreting material from a mass-loosing asymptotic giant branch (AGB) star to model the density distribution of the R Aqr system and discussed that the inclination angle between the orbital plane and the line of sight should be $i \lesssim 30°$, and Bujarrabal et al. (2021) and Alcolea et al. (2023) suggested that the best fit to the orbital parameters is $i = 20°$. Thus, we fixed the inclination to $i = 20°$. The reflection model obtained with SKIRT was converted to an additive single-parameter table (the normalization parameter $A_{\rm ref}$) using the HEASOFT[9] task `ftflx2tab`. As a summary, we list in Table 3 all the parameters of the disc structure to produce the reflection component which is further illustrated in Fig. 3.

Table 3. Details of the flared disc model obtained with SKIRT. See Fig. 3 for further details.

Parameter	Value
$r_{\rm in}$	5.4×10^{-4} au
$r_{\rm out}$	5 au
ϕ	30°
i	20°
$N_{\rm H,ref}$	5×10^{24} cm^{-2}
T	10^4 K

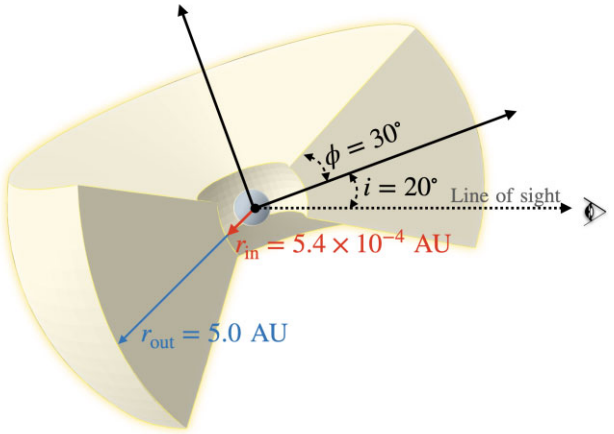

Figure 3. Representation of the accretion disc model around the WD component used in our SKIRT radiative transfer models. The diagram shows its orientation with respect to the line of sight.

[6] https://heasarc.gsfc.nasa.gov/xanadu/xspec/manual/node134.html

[7] Typical radius of WDs are estimated to be about 6000–8000 km. Here, we adopt the later value for $r_{\rm in}$.

[8] We note that Paczynski (1977) suggested that $r_{\rm out} \leq r_{\rm L}$ and the selection of $r_{\rm out} = 5$ au in fact agrees with this relationship within the error values estimated for $r_{\rm L}$.

[9] https://heasarc.gsfc.nasa.gov/docs/software/heasoft/

3.2 The best-fit models of the X-ray spectra

We adopted models in XSPEC of the form:

$$\text{tbabs}_1 \times (\text{apec}_1 + \text{apec}_2) + \text{CF} \times \text{tbabs}_3 \times (\text{apec}_3 + \text{reflection}), \quad (2)$$

where CF is a covering factor that helps alleviating the fact that the disc and the circumstellar medium around R Aqr are not homogeneous.

We first tried a single simultaneous fit to all X-ray spectra and produced an acceptable fit, but individually fitting each epoch improves the fit statistics with reduced $\chi^2_{\rm DoF}$ values between 1.07 and 1.63. The details of the different models are presented in Table 4, which lists the observed ($f_{\rm X,TOT}$) and intrinsic ($F_{\rm X,TOT}$) total fluxes and the properties of the different components for each epoch. The models and their components are compared with the background-subtracted spectra in Fig. 4.

The 2021.33–2022.78 epochs did not require the presence of the supersoft plasma component denoted as kT_1 in our model, while the rest of the earlier epochs required it to have values between $kT_1 =$ 0.02 and 0.047 keV. We attribute this situation to the reduction of the effective area of the *Chandra* ACIS instruments at soft energies. To assess the lack of the supersoft component in the later epochs, we extracted spectra of a background source located 3.93 arcmin towards the south-west from R Aqr, at $(\alpha, \delta) = (23^{\rm h}{:}43^{\rm m}{:}35\overset{\rm s}{.}96, -15^\circ{:}19'{:}16\overset{''}{.}93)$. We corroborated that this source has a significant soft flux ($E < 1.0$ keV) at epochs earlier than 2021 that is not detected in more recent observations.

The second soft component (detected in all epochs) resulted in plasma temperatures of $kT_2 \lesssim 0.2$ keV, similar to the estimates of previous works (see Sacchi et al. 2024, and references therein). The temperature of the plasma in the boundary layer varied between $kT_3 = 4$ and 12 keV, with a relatively constant plasma temperature of $kT_3 \approx 6$ keV for the 2017.78–2022.78 epochs. We particularly note that the most problematic epoch was 2000.69 because the insufficient photon statistics. The fit to this epoch required fixing kT_1 and kT_3 at 0.025 and 8.0 keV, respectively.

We illustrate in Fig. 5 the variation of the total flux $F_{\rm X,TOT}$ and that of the different components ($F_{\rm X1}$, $F_{\rm X2}$, $F_{\rm X1}$ and $F_{\rm ref}$) during the 22 yr of evolution of R Aqr.

3.3 Optical emission of the accretion disc

The extinction-corrected, flux-calibrated ARAS spectra (see Fig. 2 and Appendix A) can be used to estimate the contribution from the accretion disc to the optical emission detected from R Aqr. The first step is to subtract the contribution from the M-type star and that of the WD component from the optical spectrum of each epoch. By fitting the absorption feature at $\lambda = 6140$ Å with the templates from Fluks et al. (1994), we show that in general M8–M9 star models match the observed spectra. In contrast with the rest of the spectra, those obtained close to periastron passage (2019 November 15, 2020 January 13, 2020 January 14, 2020 January 19, and 2020 August 30) are best reproduced by M5–M6 star models (see the top panel in Figs 2, A1, and A2). However, there is still some emission above $\lambda > 6100$ Å that can not be accounted with the model. We attribute this formation and destruction of dust in the circumstellar medium close to the M-type star. Fig. 6 presents the V-magnitude light curve of R Aqr extracted from the AAVSO data base[10] that demonstrates that different optical spectra were obtained at different pulsation configurations of the M-type star.

[10] https://www.aavso.org/

The contribution from the accretion disc can be attributed to the excess of flux in the blueward part of the optical spectra. We estimated the contribution of the accretion disc to the optical flux ($F_{\rm opt}$) by subtracting the M-type star models and that of the WD component to finally integrate the residuals over the intervals $\Delta\lambda_{\rm int}$ defined in Table 2. The upper limit of the $\Delta\lambda_{\rm int}$ is defined by the exact wavelength where the observed spectrum diverges from the fitted M-type + WD component, while the lower value is defined by a common value in all ARAS spectra. This process includes an interpolation between the M-type star models and the observed spectra using cubic interpolation with the `interpolate` module from the SCIPY library in PYTHON. This was done for all ARAS spectra and the results are illustrated in Fig. 7 with grey diamonds.

The resultant flux $F_{\rm opt}$ for each ARAS spectrum was converted to luminosity ($L_{\rm opt}$), assuming a distance of 200^{+60}_{-20} pc to R Aqr. The disc optical luminosity varied between 0.08 and 0.56 $L_\odot$ for epochs between October 2017 and December 2022. $F_{\rm opt}$ and $L_{\rm opt}$ are also listed in columns 9 and 10 of Table 2, respectively.

4 DISCUSSION

4.1 The different components of the X-ray spectra

The analysis presented in the previous section helped us reveal the evolution of the global properties of R Aqr in the X-ray regime during half of its ∼22 yr binary period. In addition, it allowed us to follow in detail the behaviour of the different components. Their identification is crucial to interpret correctly the evolution of the X-ray properties of R Aqr. It is widely accepted that the heavily extinguished plasma component (in our model denoted as kT_3) is the one associated with the boundary layer, the volume between the inner region of the accretion disc and the surface of the accreting WD. Given the superb spatial resolution of *Chandra* ACIS-S (Kellogg et al. 2007; Sacchi et al. 2024), the second soft kT_2 component has been directly associated with the presence of clumps in the X-ray-emitting jet of R Aqr.

As for the supersoft kT_1 component, there is some debate on its origin in β/δ symbiotic systems. Blackbody models have been used to fit the super soft ($E = 0.3$–0.5 keV) emission from β/δ X-ray-emitting symbiotic systems arguing that this emission also arises as a result of the accretion process. Consequently, the luminosity of the supersoft component is often used to estimate the mass accretion rate (see for example Luna et al. 2018; Sacchi et al. 2024). In the case of β/δ sources, there are however two arguments against this hypothesis (see discussion in Toalá 2024). First, the hydrogen column density component of the soft emission is more consistent with that expected from the ISM along the direction of the symbiotic system. A similar situation led Mukai et al. (2007) to suggest that the supersoft component in the X-ray spectrum of CH Cyg should have an extended origin (outside the boundary layer region), very likely related to the jet seen from this symbiotic system (Galloway & Sokoloski 2004; Karovska et al. 2007). Secondly, high-resolution spectra of the supersoft X-ray component exhibit emission lines. For instance, in the symbiotic recurrent nova system T CrB, Toalá et al. (2024) demonstrated that the *XMM–Newton* RGS spectra exhibited emission lines in the supersoft range that should not be be modelled by a blackbody emission model. Consequently, we will support here the idea that the supersoft component in the X-ray spectra of R Aqr comes from extended X-ray emission produced by the variable nature of jets in symbiotic systems (see for example the case of V694 Mon in Lucy et al. 2020). In fact, Toalá et al. (2022) demonstrated that this is the case for R Aqr where the supersoft component is detected

Table 4. Parameters of the best fit models of the EPIC-pn observations of R Aqr. The fluxes were computed in the 0.3–10.0 keV and are presented in cgs units (erg cm^{-2} s^{-1}). The adopted distance is $d = 200$ pc. Bold face values represent fixed values. The normalization parameter is defined in XSPEC as $A \approx \int n_e^2 dV/4\pi d^2$, where n_e is the electron number density. Here, L_{acc} and $\dot{M}_{acc}$ are computed including L_{X3}, L_{UV}, and L_{opt} (see Section 4 for details).

Parameter	Units	2000.69	2003.99	2005.50	2005.78	2017.78	2017.79	2020.03
χ^2_{DoF}		5.33/5 = 1.07	14.20/13 = 1.09	41.50/28 = 1.48	57.76/44 = 1.31	142.95/108 = 1.32	221.45/183 = 1.21	158.42/148 = 1.07
N_{H1}	(10^{21} cm^{-2})	5.3±2.6	3.73±0.4	1.48±0.70	4.8±1.1	4.7±0.8	4.7±0.1	2.6±1.0
kT_1	(keV)	**0.025**	0.033±0.001	0.040±0.016	0.020±0.001	0.042±0.011	0.047±0.008	0.038±0.001
A_1	(cm^{-5})	390±150	3.2±1.1	0.32±0.02	14900±300	8.9±1.9	10.5±1.5	10.0±2.9
f_{X1}	(cgs)	$(2.5\pm0.9)\times10^{-15}$	$(4.9\pm1.6)\times10^{-15}$	$(9.0\pm0.5)\times10^{-14}$	$(3.6\pm0.3)\times10^{-15}$	$(6.6\pm1.1)\times10^{-14}$	$(7.7\pm0.9)\times10^{-14}$	$(2.6\pm0.7)\times10^{-13}$
F_{X1}	(cgs)	$(3.0\pm1.1)\times10^{-11}$	$(5.0\pm1.8)\times10^{-12}$	$(3.4\pm0.1)\times10^{-12}$	$(8.7\pm0.2)\times10^{-11}$	$(8.5\pm1.8)\times10^{-11}$	$(1.0\pm0.1)\times10^{-10}$	$(4.9\pm1.4)\times10^{-11}$
kT_2	(keV)	0.13±0.04	0.17±0.04	0.17±0.01	0.13±0.03	0.20±0.03	0.20±0.02	0.28±0.04
A_2	(cm^{-5})	$(2.7\pm1.9)\times10^{-4}$	$(3.0\pm2.4)\times10^{-5}$	$(8.1\pm0.8)\times10^{-5}$	$(5.9\pm1.8)\times10^{-4}$	$(6.0\pm4.4)\times10^{-4}$	$(7.0\pm3.6)\times10^{-4}$	$(2.6\pm1.6)\times10^{-4}$
f_{X2}	(cgs)	$(5.0\pm3.5)\times10^{-15}$	$(2.8\pm2.2)\times10^{-15}$	$(3.6\pm0.4)\times10^{-14}$	$(1.2\pm0.3)\times10^{-14}$	$(5.6\pm3.9)\times10^{-14}$	$(6.5\pm3.2)\times10^{-14}$	$(1.3\pm0.8)\times10^{-13}$
F_{X2}	(cgs)	$(2.2\pm1.5)\times10^{-13}$	$(4.9\pm3.8)\times10^{-14}$	$(1.4\pm0.1)\times10^{-13}$	$(6.1\pm1.9)\times10^{-13}$	$(1.2\pm0.8)\times10^{-12}$	$(1.4\pm0.6)\times10^{-12}$	$(5.7\pm3.7)\times10^{-13}$
N_{H2}	(10^{21} cm^{-2})	158.9±133.3	295.4±51.4	359.8±25.7	120.0±15.3	410±25.3	410.9±18.3	462.3±25.6
CF		0.910±0.080	0.993±0.003	0.993±0.007	0.975±0.014	0.997±0.002	0.997±0.001	0.991±0.002
kT_3	(keV)	**8.0**	4.1±1.6	11.9±5.0	10.0±8.2	6.9±0.7	6.9±0.5	6.0±0.5
A_3	(cm^{-5})	$(6.0\pm5.3)\times10^{-5}$	$(3.8\pm3.7)\times10^{-4}$	$(4.1\pm1.4)\times10^{-4}$	$(8.6\pm3.5)\times10^{-5}$	$(3.3\pm0.4)\times10^{-3}$	$(3.9\pm0.3)\times10^{-3}$	$(5.3\pm0.5)\times10^{-3}$
f_{X3}	(cgs)	$(4.5\pm4.1)\times10^{-14}$	$(1.1\pm1.0)\times10^{-13}$	$(1.8\pm0.6)\times10^{-13}$	$(6.8\pm3.0)\times10^{-14}$	$(1.1\pm0.1)\times10^{-12}$	$(1.2\pm0.2)\times10^{-12}$	$(1.5\pm0.1)\times10^{-12}$
F_{X3}	(cgs)	$(1.2\pm1.1)\times10^{-13}$	$(6.9\pm6.8)\times10^{-13}$	$(8.7\pm3.1)\times10^{-13}$	$(1.8\pm0.8)\times10^{-13}$	$(6.8\pm0.9)\times10^{-12}$	$(7.9\pm0.8)\times10^{-12}$	$(1.1\pm0.1)\times10^{-11}$
A_{ref}	(cm^{-5})	$(5.6\pm1.6)\times10^{-3}$	$(1.8\pm0.4)\times10^{-2}$	$(2.0\pm0.3)\times10^{-2}$	$(1.8\pm0.2)\times10^{-2}$	$(6.2\pm0.6)\times10^{-2}$	$(7.2\pm0.5)\times10^{-2}$	$(8.8\pm0.8)\times10^{-2}$
f_{ref}	(cgs)	$(8.6\pm2.5)\times10^{-14}$	$(2.1\pm0.4)\times10^{-13}$	$(2.1\pm0.3)\times10^{-13}$	$(2.8\pm0.3)\times10^{-13}$	$(5.7\pm0.6)\times10^{-13}$	$(6.7\pm0.4)\times10^{-13}$	$(7.5\pm0.7)\times10^{-13}$
F_{ref}	(cgs)	$(1.1\pm0.3)\times10^{-13}$	$(3.6\pm0.6)\times10^{-13}$	$(3.9\pm0.6)\times10^{-13}$	$(3.5\pm0.4)\times10^{-13}$	$(1.2\pm0.1)\times10^{-12}$	$(1.4\pm0.1)\times10^{-12}$	$(1.7\pm0.2)\times10^{-12}$
$f_{X,TOT}$	(cgs)	$(1.4\pm0.7)\times10^{-13}$	$(3.2\pm1.5)\times10^{-13}$	$(5.1\pm)\times10^{-13}$	$(3.7\pm0.6)\times10^{-13}$	$(1.8\pm0.2)\times10^{-12}$	$(2.1\pm0.5)\times10^{-12}$	$(2.6\pm0.4)\times10^{-12}$
$F_{X,TOT}$	(cgs)	$(3.0\pm1.2)\times10^{-11}$	$(6.2\pm2.5)\times10^{-12}$	$(4.8\pm0.5)\times10^{-12}$	$(8.9\pm0.2)\times10^{-11}$	$(9.4\pm1.9)\times10^{-11}$	$(1.1\pm0.2)\times10^{-10}$	$(6.2\pm1.5)\times10^{-11}$
$L_{X,TOT}$	(erg s^{-1})	$(1.4\pm0.6)\times10^{32}$	$(3.0\pm1.1)\times10^{31}$	$(2.3\pm0.2)\times10^{31}$	$(4.2\pm0.1)\times10^{32}$	$(4.5\pm0.9)\times10^{32}$	$(5.2\pm0.8)\times10^{32}$	$(2.9\pm0.7)\times10^{32}$
F_{opt}	(erg cm^{-2} s^{-1})	...	...	...	...	$(2.90\pm0.72)\times10^{-10}$	$(2.89.\pm0.72)\times10^{-10}$	$(1.57\pm0.30)\times10^{-10}$
L_{opt}	($L_\odot$)	...	...	...	...	$0.36^{+0.14}_{-0.10}$	$0.36^{+0.14}_{-0.10}$	$0.20^{+0.07}_{-0.04}$
L_{acc}	($L_\odot$)	...	...	...	...	$0.44^{+0.14}_{-0.10}$	$0.44^{+0.14}_{-0.11}$	$0.28^{+0.07}_{-0.04}$
$\dot{M}_{acc}$	($M_\odot$ yr^{-1})	...	...	...	...	$(9.9^{+4.4}_{-2.4})\times10^{-10}$	$(9.9^{+4.4}_{-2.4})\times10^{-10}$	$(6.3^{+2.5}_{-1.2})\times10^{-10}$
η	(10^{-3})	...	...	...	...	$9.9^{+4.4}_{-2.4}$	$9.9^{+4.4}_{-2.4}$	$6.3^{+2.5}_{-1.2}$
Parameter	Units	2021.33	2021.34	2022.74	2022.75	2022.76	2022.78	
χ^2_{DoF}		113.79/84=1.35	117.61/72=1.63	38.13/31=1.23	13.85/12=1.15	19.83/19=1.04	17.71/16=1.11	
N_{H1}	(10^{21} cm^{-2})	1.0±1.8	5.5±1.5	7.5±3.9	6.9±4.8	4.6±12.4	2.5±14.5	
kT_2	(keV)	0.21±0.06	0.19±0.05	0.15±0.08	0.12±0.03	0.12±0.11	0.19±0.06	
A_2	(cm^{-5})	$(1.7\pm0.2)\times10^{-4}$	$(1.2\pm1.7)\times10^{-3}$	$(6.2\pm1.0)\times10^{-3}$	$(1.8\pm0.5)\times10^{-2}$	$(9.5\pm2.2)\times10^{-3}$	$(5.3\pm1.4)\times10^{-4}$	
f_{X2}	(cgs)	$(1.6\pm0.1)\times10^{-13}$	$(6.5\pm9.5)\times10^{-14}$	$(5.2\pm0.9)\times10^{-14}$	$(4.6\pm2.2)\times10^{-14}$	$(1.3\pm0.3)\times10^{-13}$	$(9.7\pm3.8)\times10^{-14}$	
F_{X2}	(cgs)	$(3.5\pm0.4)\times10^{-13}$	$(2.2\pm3.2)\times10^{-12}$	$(8.3\pm1.4)\times10^{-12}$	$(1.3\pm0.5)\times10^{-11}$	$(7.5\pm1.8)\times10^{-12}$	$(9.0\pm3.4)\times10^{-13}$	
N_{H2}	(10^{21} cm^{-2})	511.8±43.7	332.2±31.4	473.0±57.2	468.6±9.0	444.6±69.2	551.6±87.6	
CF		0.994±0.002	0.994±0.003	0.997±0.003	0.992±0.005	0.994±0.004	0.992±0.004	
kT_3	(keV)	6.4±1.0	5.9±1.1	6.0±1.3	5.5±2.0	6.7±1.7	4.7±1.8	
A_3	(cm^{-5})	$(3.9\pm0.7)\times10^{-3}$	$(2.1\pm0.4)\times10^{-3}$	$(2.1\pm0.5)\times10^{-3}$	$(1.5\pm0.6)\times10^{-3}$	$(1.7\pm0.5)\times10^{-3}$	$(3.2\pm1.2)\times10^{-3}$	
f_{X3}	(cgs)	$(1.0\pm0.2)\times10^{-12}$	$(7.6\pm1.3)\times10^{-13}$	$(5.6\pm1.2)\times10^{-13}$	$(3.9\pm1.5)\times10^{-13}$	$(5.0\pm1.6)\times10^{-13}$	$(6.0\pm2.4)\times10^{-13}$	

Table 4 – *continued*

Parameter	Units	2000.69	2003.99	2005.50	2005.78	2017.78	2017.79	2020.03
F_{X3}	(cgs)	$(8.0\pm1.4)\times10^{-12}$	$(4.3\pm0.7)\times10^{-12}$	$(4.3\pm1.0)\times10^{-12}$	$(3.0\pm1.2)\times10^{-12}$	$(3.4\pm1.1)\times10^{-12}$	$(6.0\pm2.4)\times10^{-12}$	
A_{ref}	(cm^{-5})	0.15 ± 0.01	$(7.0\pm0.6)\times10^{-2}$	$(6.4\pm0.9)\times10^{-2}$	$(3.5\pm0.8)\times10^{-2}$	$(5.7\pm0.9)\times10^{-2}$	$(7.7\pm1.5)\times10^{-2}$	
f_{ref}	(cgs)	$(1.2\pm0.1)\times10^{-12}$	$(7.5\pm0.6)\times10^{-13}$	$(5.3\pm0.8)\times10^{-13}$	$(2.9\pm0.7)\times10^{-13}$	$(5.0\pm0.8)\times10^{-13}$	$(5.6\pm1.2)\times10^{-13}$	
F_{ref}	(cgs)	$(2.9\pm0.4)\times10^{-12}$	$(1.4\pm0.1)\times10^{-12}$	$(1.3\pm0.1)\times10^{-12}$	$(6.7\pm1.7)\times10^{-13}$	$(1.1\pm0.2)\times10^{-12}$	$(1.5\pm0.3)\times10^{-12}$	
$f_{X,TOT}$	(cgs)	$(2.4\pm0.3)\times10^{-12}$	$(1.6\pm0.3)\times10^{-12}$	$(1.1\pm0.3)\times10^{-12}$	$(7.3\pm2.3)\times10^{-13}$	$(1.1\pm0.3)\times10^{-12}$	$(1.3\pm0.3)\times10^{-12}$	
$F_{X,TOT}$	(cgs)	$(1.1\pm0.2)\times10^{-11}$	$(7.8\pm4.0)\times10^{-12}$	$(1.4\pm0.2)\times10^{-11}$	$(1.7\pm0.6)\times10^{-11}$	$(1.2\pm0.3)\times10^{-11}$	$(8.4\pm3.0)\times10^{-12}$	
$L_{X,TOT}$	(erg s^{-1})	$(5.2\pm0.9)\times10^{31}$	$(3.7\pm1.9)\times10^{31}$	$(6.7\pm1.1)\times10^{31}$	$(8.1\pm2.7)\times10^{31}$	$(5.7\pm1.5)\times10^{31}$	$(4.0\pm1.4)\times10^{31}$	
F_{opt}	(erg cm^{-2} s^{-1})	$(2.11\pm0.36)\times10^{-10}$	$(2.12\pm0.36)\times10^{-10}$	$(2.72\pm0.24)\times10^{-10}$	$(2.72\pm0.24)\times10^{-10}$	$(2.72\pm0.24)\times10^{-10}$	$(2.72\pm0.24)\times10^{-10}$	
L_{opt}	($L_\odot$)	$0.26^{+0.01}_{-0.05}$	$0.27^{+0.01}_{-0.05}$	$0.34^{+0.11}_{-0.05}$	$0.34^{+0.11}_{-0.05}$	$0.34^{+0.11}_{-0.05}$	$0.34^{+0.11}_{-0.05}$	
L_{acc}	($L_\odot$)	$0.34^{+0.09}_{-0.05}$	$0.34^{+0.09}_{-0.05}$	$0.41^{+0.11}_{-0.05}$	$0.41^{+0.11}_{-0.05}$	$0.41^{+0.11}_{-0.05}$	$0.41^{+0.11}_{-0.05}$	
$\dot{M}_{acc}$	($M_\odot$ yr^{-1})	$(7.7^{+3.1}_{-1.4})\times10^{-10}$	$(7.7^{+3.1}_{-1.4})\times10^{-10}$	$(9.3^{+3.7}_{-1.4})\times10^{-10}$	$(9.3^{+3.7}_{-1.4})\times10^{-10}$	$(9.3^{+3.7}_{-1.4})\times10^{-10}$	$(9.4^{+3.7}_{-1.4})\times10^{-10}$	
η	(10^{-3})	$7.7^{+3.1}_{-1.4}$	$7.6^{+3.1}_{-1.4}$	$9.3^{+3.7}_{-1.4}$	$9.3^{+3.7}_{-1.4}$	$9.3^{+3.7}_{-1.4}$	$9.4^{+3.7}_{-1.4}$	

as an extended emission permeating the nebula associated with this symbiotic system.

There is no doubt that the presence of the 6.4 keV Fe emission line in symbiotic systems is produced by reflecting material in the vicinity of the boundary layer (e.g. Eze 2014). Nevertheless, very little effort has been done in the literature in order to produce physically driven models that fit this component and the best way to avoid this is to include a Gaussian profile to fit the 6.4 keV Fe emission line. Following the methodology by our group, here we have proposed that the reflecting material is the accretion disc. We estimated the effective Roche lobe radius of $4.7^{+1.4}_{-0.5}$ au which resulted to be very similar to the estimations of 5 au presented by the analysis of near-IR data in Hinkle et al. (2022). Consequently, our flared disc model was created with an outer radius of 5 au. In contrast, the radius of the M-type star is estimated to be about 250 $R_\odot$ ($\lesssim$1.2 au) and might not fill its Roche lobe to create an accretion disc. The formation of the accretion disc might alternatively proceed through a Bondi–Hoyle–Lyttleton process (Hoyle & Lyttleton 1939; Bondi & Hoyle 1944) or wind Roche lobe overflow mechanism (Podsiadlowski & Mohamed 2007; de Val-Borro, Karovska & Sasselov 2009).

Although the accretion disc should be the main source of reflection, given its larger density (see e.g. Lee, Kim & Lee 2022), other structures in its vicinity might be able to contribute to the reflection component to a lesser extent. For example simulations of accreting WDs show the formation of large scale ($\gtrsim$100 au) 3D spiral structures (de Val-Borro et al. 2017; Liu et al. 2017). Those structures will be best included in further studies by applying the radiative-transfer code SKIRT to the density structures obtained from hydrodynamical simulations.

4.2 Consequences of the spectral analysis

Based on the models obtained from the multiple *Chandra* and *XMM–Newton* observations of R Aqr, we found that during the period from 2000.69 to 2022.78, the total intrinsic X-ray flux $F_{X,TOT}$ exhibited a certain degree of variability (see Fig. 5), with an estimated median flux of 1.4×10^{-11} erg s^{-1} cm^{-2}, and a median absolute deviation of 7.8×10^{-12} erg s^{-1} cm^{-2}, without a clear increasing nor decreasing trend. Almost exactly the same behaviour is observed for the supersoft component F_{X1}, a characteristic that demonstrates that it dominates the total intrinsic flux. The non-detection of this component beyond 2021.33 has to be attributed to the ACIS instrument's dramatic reduction of effective area in the soft energy range (<1.0 keV) rather than to its intrinsic decline. On the other hand, the second soft component F_{X2}, exhibits a flux increase from the first to the last epoch of observation ranging about 2 orders of magnitude. Given that the kT_2 plasma component can be directly associated with X-ray-emitting clumps in the jet, it might be suggested that the jet activity increased with the system approaching periastron passage (see Sacchi et al. 2024).

We also report a direct correlation between the evolution of the flux of the boundary layer F_{X3} and the periastron passage of the stellar components of R Aqr. Fig. 5 shows that the lower F_{X3} values correspond approximately to apastron passage (about the year 2000), but it peaks at periastron passage (∼2019.9). After this, the flux of the boundary layer started declining. This pattern might be related to the variation of the efficiency of the accretion process as R Aqr approaches periastron passage. We note that a similar behaviour is exhibited by the reflection component, although not exactly the same. For example the peak of the reflection component does not corresponds exactly to the periastron passage, but a couple of years after it.

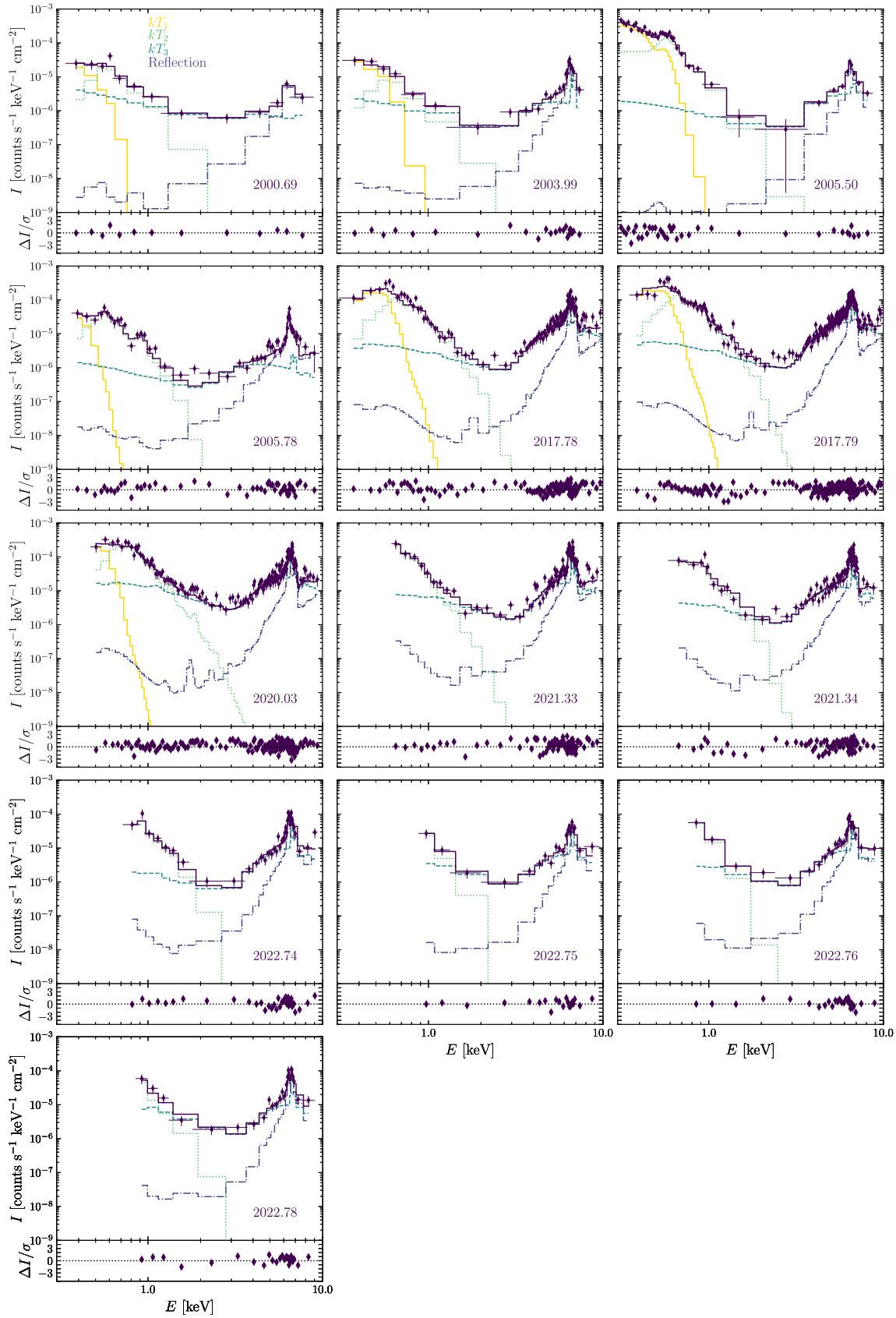

Figure 4. Background-subtracted X-ray spectra of R Arq. Different panels show details of the best-fit models for each epoch. The contribution from the different components to each epoch are shown. See details in Table 4.

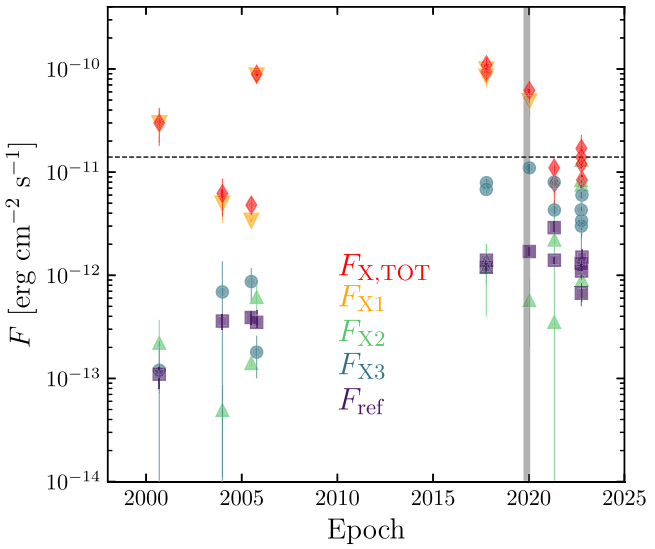

Figure 5. Evolution with time of the intrinsic X-ray flux in R Aqr. Different symbols show the evolution of the total flux ($F_{\rm X,TOT}$ – diamonds), the contribution from the soft components ($F_{\rm X1}$ and $F_{\rm X2}$ – triangles), the boundary layer plasma ($F_{\rm X3}$ – bullets), and that of the reflection ($F_{\rm ref}$ – squares). The vertical shaded area shows the approximate dates of the periastron passage (2019.9±0.1), while the horizontal dashed line represents the estimated median value of 1.4×10^{-11} erg cm^{-2} s^{-1} for $F_{\rm X,TOT}$.

It is important to note here that the 2021 and 2022 *Chandra* observations were obtained with only a few days of difference among them, yet some variation is detected. For example the 2021.33 and 2021.34 observations, obtained within 1 d, exhibit subtle but clear differences (see Table 4 and Fig. 5). The same can be stated about the 2022 observations. This situation shows that the X-ray emission from R Aqr is variable within time-scales of days.

Finally, we would like to remark that the *XMM–Newton* and *Chandra* observations analysed here are limited to the 0.3–10.0 keV range, but it is well-known that symbiotic systems may emit X-ray emission at higher energies, up to 100 keV (e.g. Luna et al. 2019). Previous analyses of *Swift* data of symbiotic systems require extremely high plasma temperatures in order to fit the high energetic part of their spectra ($kT \lesssim 30$ keV; Kennea et al. 2009). Nevertheless, recent analysis of multi-epoch observations of the symbiotic recurrent nova system T CrB including reflection from an accretion disc do not require such high plasma temperatures. According to the models presented in Toalá et al. (2024), reflection dominates the 15–50 keV energy range in T CrB. We note that such spectra resemble those emitted by an active galactic nucleus in which a Compton shoulder is one of the main components (e.g. Kaspi et al. 2002). However, in the case of symbiotic systems this feature is purely modelled by the combination of the plasma component from the boundary layer and the reflection. In Fig. 8, we present the predictions for the 3.0–50.0 keV energy range from our best-fit model to the 2017.78 *Chandra* observations. This model predicts that reflection in R Aqr should dominate the 10.0–50.0 keV energy range but, unfortunately, there are no available X-ray observations in this energy range to compare with. Future observations covering this energy range, such as those provided by *NuSTAR*, are necessary in order to corroborate or improve the accuracy of the reflection models presented here.

4.3 The evolution of $\dot{M}_{\rm acc}$

Fig. 7 illustrates the evolution of the optical flux from the accretion disc, which is found to be somewhat constant for a time period ∼3 yr before and after periastron passage.

Since X-ray and optical observations are not contemporaneous, we apply a Gaussian process (GP; Rasmussen & Williams 2006) to generate a non-parametric model, which is evaluated at the X-ray epochs. This Bayesian statistical approach fits the data using a constant mean function and a covariance matrix. We used the PYTHONGPflow library,[11] with a squared exponential kernel (Wilson & Adams 2013), which we consider appropriate for describing the data correlation. By applying this model, we can sample $F_{\rm opt}$ at the epochs of the X-ray observations. These values are listed in Table 4 represented by the parameter $L_{\rm opt}$, along with their respective uncertainties derived and propagated from the GP covariance matrix and the uncertainty in the distance. These fluxes are illustrated in Fig. 7 with triangles.

Previous works have tried to correlate the optical and the X-ray emission, for example, we note the classic work of Patterson & Raymond (1985), where theoretical models of accreting WDs are compared with observations. However, those works adopt the complete X-ray luminosity in order to estimate accretion mass-loss rates, but we advise against that method (see above). The ratio of the X-ray flux from the boundary layer and the optical flux from the accretion disc has values of $F_{\rm X3}/F_{\rm opt} \approx 0.03$, ≈ 0.07, and $\lesssim 0.02$ prior, during, and after periastron passage (see top panel of Fig. 9). According to the theoretical predictions from Patterson & Raymond (1985), the peak of the $F_{\rm X3}/F_{\rm opt}$ would suggest a mass accretion rate on to the WD of $\dot{M}_{\rm acc} \approx 10^{17}$ g s^{-1}($\approx 10^{-9}$ M$_\odot$ yr^{-1}).

On the other hand, assuming that the total accretion luminosity $L_{\rm acc}$ originates from a standard thin accretion disc (Shakura & Sunyaev 1973; Pringle 1981), we can express it as

$$L_{\rm acc} = \frac{1}{2}\frac{GM_{\rm WD}}{R_{\rm WD}}\dot{M}_{\rm acc}, \quad (3)$$

with G as the gravitational constant and $R_{\rm WD}$ the radius of the WD component, where $L_{\rm acc}$ should be the bolometric luminosity produced by the accretion process. That is, $L_{\rm acc}$ should account for all the emission produced (at least) in the optical and X-ray regime. Moreover, given the fact that symbiotic systems also emit considerably in the UV (see for example Guerrero et al. 2024, and references therein) we tried to assess the contribution of the accretion disc to this wavelength range.

Unfortunately, there are no contemporary spectroscopic UV observations of R Aqr. Appendix B describes our attempt to estimate an averaged contribution from the accretion disc into the near-UV range using available *IUE* observations. We calculated a median spectrum for all the *IUE* data available in the Mikulski Archive for Space Telescopes (MAST).[12] A blackbody model fitted to the near-UV median spectrum resulted in $T_{\rm bb} = 25\,000$ K, $L_{\rm WD} = 0.19^{+0.11}_{-0.04}$ L$_\odot$, and $R_{\rm WD} = 0.025^{+0.008}_{-0.003}$ R$_\odot$ (see details in Appendix B). After subtracting this model to the near-UV spectrum, we estimate an excess of $L_{\rm UV} = 0.07^{+0.04}_{-0.01}$ L$_\odot$ which can be attributed to the accretion disc. We note that although the different *IUE* near-UV spectra might suggest a certain degree of variability, the median spectrum presented in Fig. B1 seems to be a good representation of the averaged properties.

[11] https://www.gpflow.org/
[12] https://archive.stsci.edu/

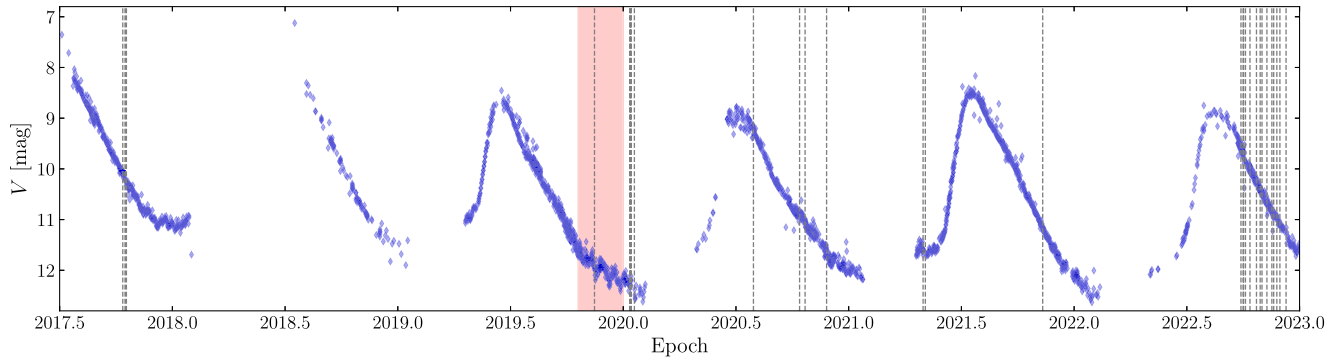

Figure 6. Light curve (diamonds) in the Johnson V band filter of R Aqr extracted from the AAVSO data base. The dashed vertical lines illustrate the dates of acquisition of the ARAS spectra and the X-ray observations. The shaded region marks the periastron passage (2019.9+0.1). The figure illustrates that the observations obtained at the beginning of 2020 correspond to minimum in the pulsation of the M-type star component of R Aqr.

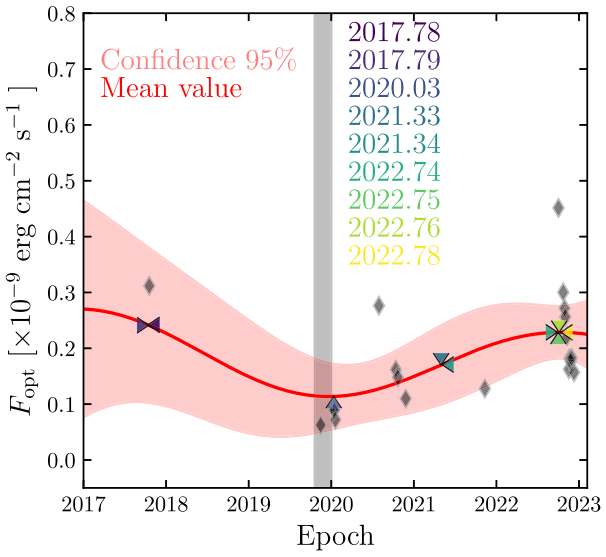

Figure 7. Evolution of the optical flux of the accretion disc ($F_{\rm opt}$) estimated from the ARAS spectra (diamonds). The line represents the mean function while the shaded region indicates the confidence interval derived from the covariance matrix of the Gaussian process fit (see Section 4.3 for details). The triangles correspond to the epochs of X-ray observations. To avoid confusion, each triangle is used as an arrow head to point to the referred value.

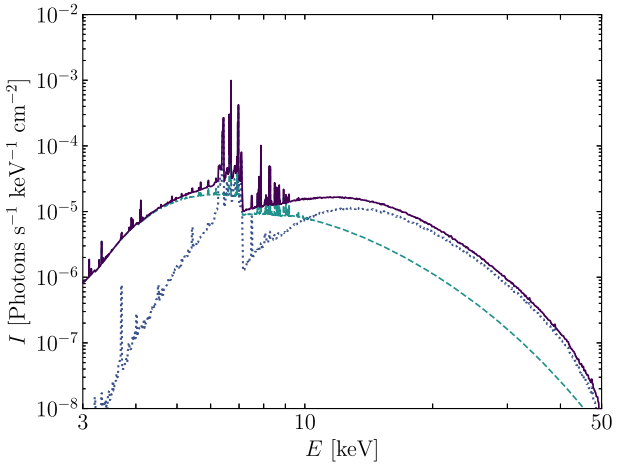

Figure 8. Predictions for the hard energy range of our reflection model for the 2017.78 epoch of observations of R Aqr (solid line). The dashed and dotted lines illustrate the contribution from the plasma temperature of the boundary layer (kT_3) and that of reflection, respectively.

We then proceeded to calculate the mass accretion rate using equation (3) and adopting $L_{\rm acc} = L_{\rm opt} + L_{\rm UV} + L_{\rm X3}$ with $R_{\rm WD}$ =0.025 R$_\odot$. With these corrections, we now estimate the mass accretion rate to have values around $\dot{M}_{\rm acc} \approx [0.6 - 1] \times 10^{-9}$ M$_\odot$ yr^{-1} for the epoch interval from 2017.78 to 2022.78. The exact values are presented in Table 4 as $\dot{M}_{\rm acc}$ and are illustrated in the bottom panel of Fig. 9. The lowest $\dot{M}_{\rm acc}$ value corresponds to the 2020.03 epoch reflecting the behaviour of the optical luminosity of the accretion disc $L_{\rm opt}$, which is the dominant wavelength.

It is important to note here that the contribution of X-rays from the boundary layer ($L_{\rm X3}$) to the total bolometric luminosity produced by accretion ($L_{\rm acc}$) is small compared to the optical and UV fluxes of the accretion disc, given that, $L_{\rm X3} \approx [10^{-4}$–$10^{-2}]$ L$_\odot$ (see Table 4). Thus, for the specific case of R Aqr, we can approximate $\dot{M}_{\rm acc}$ by simply accounting for the optical and UV contribution from the accretion disc. That is, by assuming $L_{\rm acc} = L_{\rm opt} + L_{\rm UV}$. Consequently, in Fig. 10, we present the $\dot{M}_{\rm acc}$ estimations for all epochs of the ARAS spectra. Again, Fig. 10 shows the results from applying a Gaussian process to the estimated accretion rates and efficiencies derived from equation (3). The solid (blue) line represents the mean function (the most likely values given a realization of the model), while the shaded region indicates the confidence interval associated with the covariance matrix of the Gaussian process fit. Fig. 10 shows that from 2017 to 2023 the mass accretion rate $\dot{M}_{\rm acc}$ exhibits a certain degree of variability, with a median value of 7.3×10^{-10} M$_\odot$ yr^{-1}.

For comparison, we mention that there are different estimations for the mass accretion rate on to the WD in R Aqr. Depending on a combination of different parameters, such as $M_{\rm WD}$, $R_{\rm WD}$, the disc temperature and the efficiency of the accreted Mira-type wind on to the WD, Burgarella et al. (1992) estimated different $\dot{M}_{\rm acc}$ values ranging from 1.8×10^{-9} to 3.1×10^{-8} M$_\odot$ yr^{-1}. Other works (see e.g. Henney & Dyson 1992; Ragland et al. 2008; Melnikov et al. 2018) assumed that $\dot{M}_{\rm acc}$ should be about 10 per cent or an order of magnitude lower than the mass-loss rate of the red giant component, which has been estimated to be $\dot{M}_{\rm Mtype} \approx 10^{-7}$ M$_\odot$ yr^{-1} from radio wavelengths (Michalitsianos, Kafatos & Hobbs 1980; Spergel, Giuliani & Knapp 1983; Hollis et al. 1985). We note

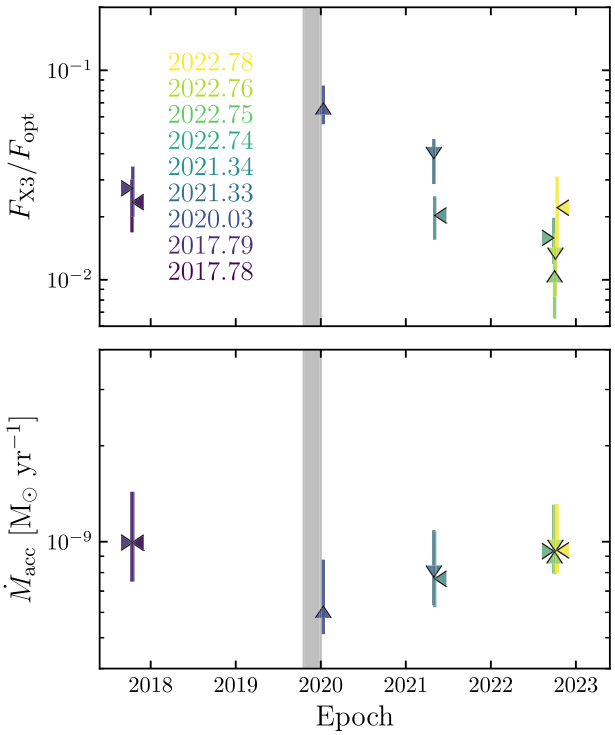

Figure 9. Evolution with time of the ratio of the X-ray emission from the boundary layer F_{X3} over the optical flux of the accretion disc F_{opt} (*top panel*) and the mass accretion rate $\dot{M}_{acc}$ (*bottom panel*). The shaded grey area represents the periastron passage (2019.9±0.1). To avoid any confusion the triangles are oriented as arrowheads, pointing towards the value obtained for each epoch.

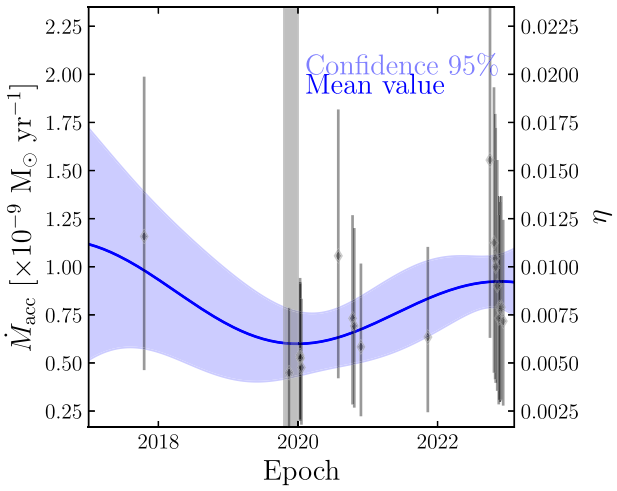

Figure 10. Evolution of the mass accretion rate $\dot{M}_{acc}$ estimated by adopting only the optical L_{opt} and UV L_{UV} emission from the accretion disc (left vertical axis) and the wind accretion efficiency η (left vertical axis). The shaded region and the solid line result from the Gaussian process applied to the data and provide an idea of the behaviour in the intervals without data.

that previous mass accretion rate estimates adopted a total luminosity for the boundary layer and the disc of 10 $L_\odot$, a value that is about 2 orders of magnitude larger than our luminosity estimates.

Fig. 10 also shows the evolution of the mass accretion efficiency η, which is defined as

$$\eta = \frac{\dot{M}_{acc}}{\dot{M}_{Mtype}}. \quad (4)$$

The evolution of R Aqr suggest efficiency values from $\eta = 4.49 \times 10^{-3}$ up to $\eta = 1.55 \times 10^{-2}$, with a median value of 7×10^{-3}, as estimated from $\dot{M}_{acc}$ values presented in the Table 2. The minimum η values are obtained for epochs around the periastron passage of R Aqr, but we attribute this to the coincidence of a pulsation minimum of the M-type star (see Fig. 6).

In Appendix C, we present an analytical model to study the accretion luminosity L_{acc} evolution for a system with the same observed properties of R Aqr. This model incorporates a reformulated Bondi–Hoyle–Lyttleton accretion mechanism, which will be comprehensively detailed and validated against other observations and simulations in Tejeda & Toalá (2024). Our analytical model suggests that the observations can be reasonably reproduced by a M-type star with a mass-loss rate of $\dot{M}_{Mtype} = 10^{-7}$ $M_\odot$ yr^{-1} and wind velocities between 25 and 40 km s^{-1} as illustrated by the top panel of Fig. C2 (consistent with wind properties of evolved stars; see e.g. Ramstedt et al. 2020). For these wind parameters, our model predicts mass accretion efficiencies between $\eta = 4.77 \times 10^{-3}$ and 1.64×10^{-2}, consistent with the observationally derived values. The bottom panel of this figure shows similar calculations adopting different $\dot{M}_{Mtype}$ values. This seems to suggest that the variable observed properties of R Aqr can be attributed to the variable nature of the wind properties of the Mira-type star; a property that is not incorporated in the current analytical predictions. The analytical solution predicts that the peak mass accretion rate occurs shortly after periastron passage. For example with a wind velocity of 30 km s^{-1}, the maximum is reached 1.8 yr after periastron, around 2021.7 (see Fig. C2).

5 SUMMARY AND CONCLUSIONS

We presented the analysis of multi-epoch *Chandra* ACIS-S and *XMM–Newton* EPIC pn X-ray observations of the symbiotic system R Aqr. The observations cover about 22 yr of evolution of this symbiotic system, between 2000 and 2022, about half of the orbital period of the system. We corroborated that R Aqr remained a β/δ-type X-ray-emitting symbiotic system but with a certain degree of flux variation. We analysed the X-ray spectra including a reflection model, instead of the oft-used Gaussian component to fit the 6.4 keV Fe emission line. This model allows us to dissect the different contributing components to the X-ray spectra: the soft extended emission from the jet, the heavily extinguished plasma component of the boundary layer, and the contribution from reflection that naturally includes the 6.4 keV Fe fluorescent line. In addition, we analysed publicly available optical and UV data to study the properties of the accretion disc. All our estimates were computed adopting a distance to R Aqr of $d = 200^{+60}_{-20}$ pc.

Our main findings can be summarized as follows:

(i) Driven by recent description of the orbital parameters of the binary system in R Aqr, we constructed a reflecting structure with a flared disc geometry with inner and outer radii of $r_{in} = 5 \times 10^{-4}$ and $r_{out} = 5$ au, respectively, and an inclination of 20° with respect to the line of sight. The disc is characterized by an averaged column density of $N_{H,ref} = 5 \times 10^{24}$ and a temperature of $T = 10^4$ K. The size of this disc structure is significantly smaller than the estimated radius of the M-type component, which lead us to suggest that the

accretion process might be due to a Bondi–Hoyle-like process or a wind Roche lobe overflow scenario.

(ii) The intrinsic total flux ($F_{\rm X,TOT}$) and luminosity ($L_{\rm X,TOT}$) computed for the 0.3–10.0 keV energy range exhibited some degree of variation, but in general, we found that these varied around median values for $F_{\rm X,TOT} = 1.4\times10^{-11}$ erg s^{-1} cm^{-2} and $L_{\rm X,TOT} = 6.7\times10^{31}$ erg s^{-1}. On the other hand, the different components exhibit dramatic variations during the 22 yr of observations.

(iii) We found that the flux from the boundary layer ($F_{\rm X3}$) and that of the reflection component ($F_{\rm ref}$) are tightly correlated to the periastron passage. They exhibit their minimum values 21 yr before periastron passage, a maximum is achieved during periastron, and then their fluxes started to decline. We predict that the fluxes of these two components will keep on declining for another ∼21 yr after periastron (assuming that the period of the symbiotic system is in fact 42 yr). A similar behaviour, but with larger uncertainties, is exhibited by the second soft component kT_2 attributed to the presence of hot X-ray-emitting pockets of gas produced by the precessing jet in R Aqr.

(iv) The supersoft component (kT_1) dominates the total flux for epochs before 2021, then it is not detected in the last *Chandra* observations. We attribute this situation to the diminishing of the effective area of the *Chandra* ACIS-S detectors and not to an intrinsic disappearance of the supersoft component. This situation was corroborated by evaluating the spectra of other sources in the vicinity of R Aqr.

(v) We modelled publicly available optical spectra from the ARAS data base for epochs covering the October 2017 to December 2022. The spectra were analysed to subtract the contribution from the M-type and the WD components of R Aqr to estimate the contribution from the accretion disc to the optical ($L_{\rm opt}$). We estimate that its optical luminosity varied between 0.08 and 0.56 L$_\odot$ during these epochs.

(vi) Using available near-UV data from the *IUE* satellite, we estimated the properties of the WD component in R Aqr. Our analysis of the median near-UV spectrum resulted in a blackbody component with $T_{\rm bb} = 25{,}000$ K, radius $R_{\rm WD} = 0.025^{+0.008}_{-0.003}$ R$_\odot$, and $L_{\rm WD} = 0.19^{+0.11}_{-0.04}$ L$_\odot$. This helped us estimate that the accretion disc has a contribution of $L_{\rm UV} = 0.07^{+0.04}_{-0.01}$ L$_\odot$ in the near-UV.

(vii) We estimated mass accretion rates $\dot{M}_{\rm acc}$ accounting for the optical, UV, and X-ray emission produced by the accretion process, but we notice that the X-ray emission from the boundary layer does not contribute significantly to the total $L_{\rm acc}$. Thus, $\dot{M}_{\rm acc}$ was also computed accounting only for the optical and UV emission from the accretion disc. We found that $\dot{M}_{\rm acc}$ varied around a median value of 7.3×10^{-10} M$_\odot$ yr^{-1}. Adopting a mass-loss rate of $\dot{M}_{\rm Mtype} = 1\times10^{-7}$ M$_\odot$ yr^{-1}, we were able to estimate the wind accretion efficiency, which we defined as $\eta = \dot{M}_{\rm acc}/\dot{M}_{\rm Mtype}$. This efficiency parameter resulted in values between 4.49×10^{-3} and 1.55×10^{-2} with a median value of 7×10^{-3}.

(viii) Our results align well with predictions from an analytical Bondi–Hoyle–Lyttleton accretion model using the same orbital parameters. Notably, the observed variability in disc luminosity is consistent with the model's predictions for wind velocities between 25 and 40 km s^{-1}. Furthermore, the model predicts a mass accretion efficiency at periastron consistent with those predicted from observations.

(ix) We made predictions for the higher energy range (E >10–50 keV) and noticed that the reflection component will dominate the hard X-ray emission. Future observations such as those provided by *NuStar* can help assessing the role of the reflection disc in R Aqr.

ACKNOWLEDGEMENTS

The authors thank the referee, Radoslav Zamanov, for comments and suggestions that improved our analysis and the presentation of our results. JAT and DAVT acknowledge support from the UNAM PAPIIT project IN102324. DAVT thanks Consejo Nacional de Humanidades, Cientica y Tecnología (CONAHCyT, Mexico) for a student grant. MAG acknowledges financial support from grants CEX2021-001131-S funded by MCIN/AEI/10.13039/501100011033 and PID2022-142925NB-I00 from the Spanish Ministerio de Ciencia, Innovación y Universidades (MCIU) cofunded with FEDER funds. The authors thank Cesar Eduardo Feliciano Torres for the 3D model used to create the sketch of the flared disc. MK acknowledges the support provided via the NASA Chandra grants DD9- 20111X, GO1-22027X, and GO-24014. This paper employs a list of *Chandra* data sets, obtained by the NASA Chandra X-ray Observatory. We acknowledge with thanks the variable star observations from the AAVSO International Database contributed by observers worldwide and used in this research. We are grateful to the ARAS team for the spectra used in this research. This work has made extensive use of NASA's Astrophysics Data System (ADS).

DATA AVAILABILITY

The data underlying this work are available in public archives as described in Section 2. The processed observations files will be shared on reasonable request to the first author.

REFERENCES

Alcolea J. et al., 2023, in Manteiga M., eds, et al., Proceedings of the XV Scientific Meeting of the Spanish Astronomical Society, Highlights of Spanish Astrophysics XI. La Laguna, Spain, p. 190
Arnaud K. A., 1996, Astron. Data Anal. Softw. Syst. V., 101, 17
Bailer-Jones C. A. L., Rybizki J., Fouesneau M., Demleitner M., Andrae R., 2021, AJ, 161, 147
Bondi H., Hoyle F., 1944, MNRAS, 104, 273
Bujarrabal V., Alcolea J., Mikołajewska J., Castro-Carrizo A., Ramstedt S., 2018, A&A, 616, L3
Bujarrabal V., Agúndez M., Gómez-Garrido M., Kim H., Santander-García M., Alcolea J., Castro-Carrizo A., Mikolajewska J., 2021, A&A, 651, A4
Burgarella D., Vogel M., Paresce F., 1992, A&A, 262, 83
Camps P., Baes M., 2020, Astron. Comput., 31, 100381
Cardelli J. A., Clayton G. C., Mathis J. S., 1989, ApJ, 345, 245
de Val-Borro M., Karovska M., Sasselov D. D., 2009, ApJ, 700, 1148
de Val-Borro M., Karovska M., Sasselov D. D., Stone J. M., 2017, MNRAS, 468, 3408
Eggleton P. P., 1983, ApJ, 268, 368
Eze R. N. C., 2014, MNRAS, 437, 857
Fruscione A. et al., 2006, in Silva D. R., Doxsey R. E, eds, Proc. SPIE Conf. Ser. Vol. 6270, Observatory Operations: Strategies, Processes, and Systems. SPIE, Bellingham, p. 62701V
Fluks M. A., Plez B., The P. S., de Winter D., Westerlund B. E., Steenman H. C., 1994, A&AS, 105, 311
Gabriel C. et al., 2004, Astron. Data Anal. Softw. Syst. XIII., 314, 759
Galloway D. K., Sokoloski J. L., 2004, ApJ, 613, L61
Gromadzki M., Mikołajewska J., 2009, A&A, 495, 931
Guerrero M. A., Montez R., Ortiz R., Toalá J. A., Kastner J. H., 2024, A&A, 689, A62
Henney W. J., Dyson J. E., 1992, A&A, 261, 301
Hinkle K. H., Brittain S., Fekel F. C., Lebzelter T., Boogert A., 2022, ApJ, 937, 98
Hollis J. M., Kafatos M., Michalitsianos A. G., McAlister H. A., 1985, ApJ, 289, 765
Hoyle F., Lyttleton R. A., 1939, Proc. Camb. Philos. Soc., 35, 405

Huang C. D., Karovska M., Hack W., Raymond J. C., Montez R., Jr, Kashyap V. L., 2023, ApJ, 947, 11
Hunsch M., Schmitt J. H. M. M., Schroder K.-P., Zickgraf F.-J., 1998, A&A, 330, 225
Ishida M., Okada S., Hayashi T., Nakamura R., Terada Y., Mukai K., Hamaguchi K., 2009, PASJ, 61, S77
Jura M., Helfand D. J., 1984, ApJ, 287, 785
Karovska M., Carilli C. L., Raymond J. C., Mattei J. A., 2007, ApJ, 661, 1048
Kaspi S. et al., 2002, ApJ, 574, 643
Kellogg E., Anderson C., Korreck K., DePasquale J., Nichols J., Sokoloski J. L., Krauss M., Pedelty J., 2007, ApJ, 664, 1079
Kellogg E., Pedelty J. A., Lyon R. G., 2001, ApJ, 563, L151
Kennea J. A., Mukai K., Sokoloski J. L., Luna G. J. M., Tueller J., Markwardt C. B., Burrows D. N., 2009, ApJ, 701, 1992
Lamers H. J. G. L. M., Cassinelli J. P., 1999, in Lamers H. J. G. L. M., Cassinelli J. P., eds, Introduction to Stellar Winds. Cambridge Univ. Press, Cambridge, p. 452
Lee Y.-M., Kim H., Lee H.-W., 2022, ApJ, 931, 142
Liimets T. et al., 2018, A&A, 612, A118
Linford J. D. et al., 2019, ApJ, 884, 8
Liu Z.-W., Stancliffe R. J., Abate C., Matrozis E., 2017, ApJ, 846, 117
Lodders K., Palme H., Gail H.-P., 2009, Landolt Börnstein, 4B, 712
Lopes de Oliveira R., Sokoloski J. L., Luna G. J. M., Mukai K., Nelson T., 2018, ApJ, 864, 46
Lucy A. B. et al., 2020, MNRAS, 492, 3107
Luna G. J. M., Sokoloski J. L., Mukai K., Nelson T., 2013, A&A, 559, A6
Luna G. J. M. et al., 2018, A&A, 619, A61
Luna G. J. M., Nelson T., Mukai K., Sokoloski J. L., 2019, ApJ, 880, 94
Melnikov S., Stute M., Eislöffel J., 2018, A&A, 612, A77
Michalitsianos A. G., Kafatos M., Hobbs R. W., 1980, ApJ, 237, 506
Mikolajewska J., Kenyon S. J., 1992, AJ, 103, 579
Mikolajewska J., Acker A., Stenholm B., 1997, A&A, 327, 191
Mukai K., 2017, PASP, 129, 062001
Mukai K., Ishida M., Kilbourne C., Mori H., Terada Y., Chan K.-W., Soong Y., 2007, PASJ, 59, 177
Paczynski B., 1977, ApJ, 216, 822
Patterson J., Raymond J. C., 1985, ApJ, 292, 535
Podsiadlowski P., Mohamed S., 2007, Baltic Astron., 16, 26
Pringle J. E., 1981, ARA&A, 19, 137
Ragland S. et al., 2008, ApJ, 679, 746
Ramstedt S. et al., 2020, A&A, 640, A133
Rasmussen C. E., Williams C. K. I., 2006, Gaussian Processes for Machine Learning. MIT Press, Cambridge, MA
Sacchi A. et al., 2024, ApJ, 961, 12
Saladino M. I., Pols O. R., van der Helm E., Pelupessy I., Portegies Zwart S., 2018, A&A, 618, A50
Santamaría E., Toalá J. A., Liimets T., Guerrero M. A., Botello M. K., Sabin L., Ramos-Larios G., 2024, MNRAS, 532, 2511
Shakura N. I., Sunyaev R. A., 1973, A&A, 24, 337
Sion E. M., Godon P., Mikolajewska J., Katynski M., 2019, ApJ, 874, 178
Snaid S., Zijlstra A. A., McDonald I., Barker H., Marsh T. R., Dhillon V. S., 2018, MNRAS, 477, 4200
Spergel D. N., Giuliani J. L., Knapp G. R., 1983, ApJ, 275, 330
Tejeda E., Toalá J. A., 2024, preprint (arXiv:2411.01755)
Teyssier F., 2019, Contrib. Astron. Obs. Skalnate Pleso., 49, 217
Theuns T., Boffin H. M. J., Jorissen A., 1996, MNRAS, 280, 1264
Toalá J. A., 2024, MNRAS, 528, 987
Toalá J. A., González-Martín O., Karovska M., Montez R., Botello M. K., Sabin L., 2023, MNRAS, 522, 6102
Toalá J. A., González-Martín O., Sacchi A., Vasquez-Torres D. A, 2024, MNRAS, 532, 1421
Toalá J. A., Sabin L., Guerrero M. A., Ramos-Larios G., Chu Y.-H., 2022, ApJ, 927, L20
Tody D., 1993, Astron. Data Anal. Softw. Syst. II., 52, 173
Vander Meulen B. et al., 2023, A&A, 674, A1
Vassiliadis E., Wood P. R., 1993, ApJ, 413, 641
Viotti R., Piro L., Friedjung M., Cassatella A., 1987, ApJ, 319, L7
Wilms J., Allen A., McCray R., 2000, ApJ, 542, 914
Wilson A., Adams R., 2013, in Dasgupta S., McAllester D., eds, Proceedings of the 30th International Conference on Machine Learning, Vol. 28, No. 3. PMLR, Atlanta, GA, p. 1067
Zhekov S. A., Tomov T. V., 2019, MNRAS, 489, 2930

APPENDIX A: ARAS SPECTRA

We present in Figs A1 and A2 the extinction-corrected, flux-callibrated ARAS spectra listed in Table 2. Different panels show individual spectra as well as the profiles of stellar spectra of M-type stars from Fluks et al. (1994) what were used to estimate the disc luminosity in the optical band ($L_{\rm opt}$). All spectra have been corrected for extinction adopting $A_{\rm V} = 0.1$ mag and the Cardelli et al. (1989) extinction law.

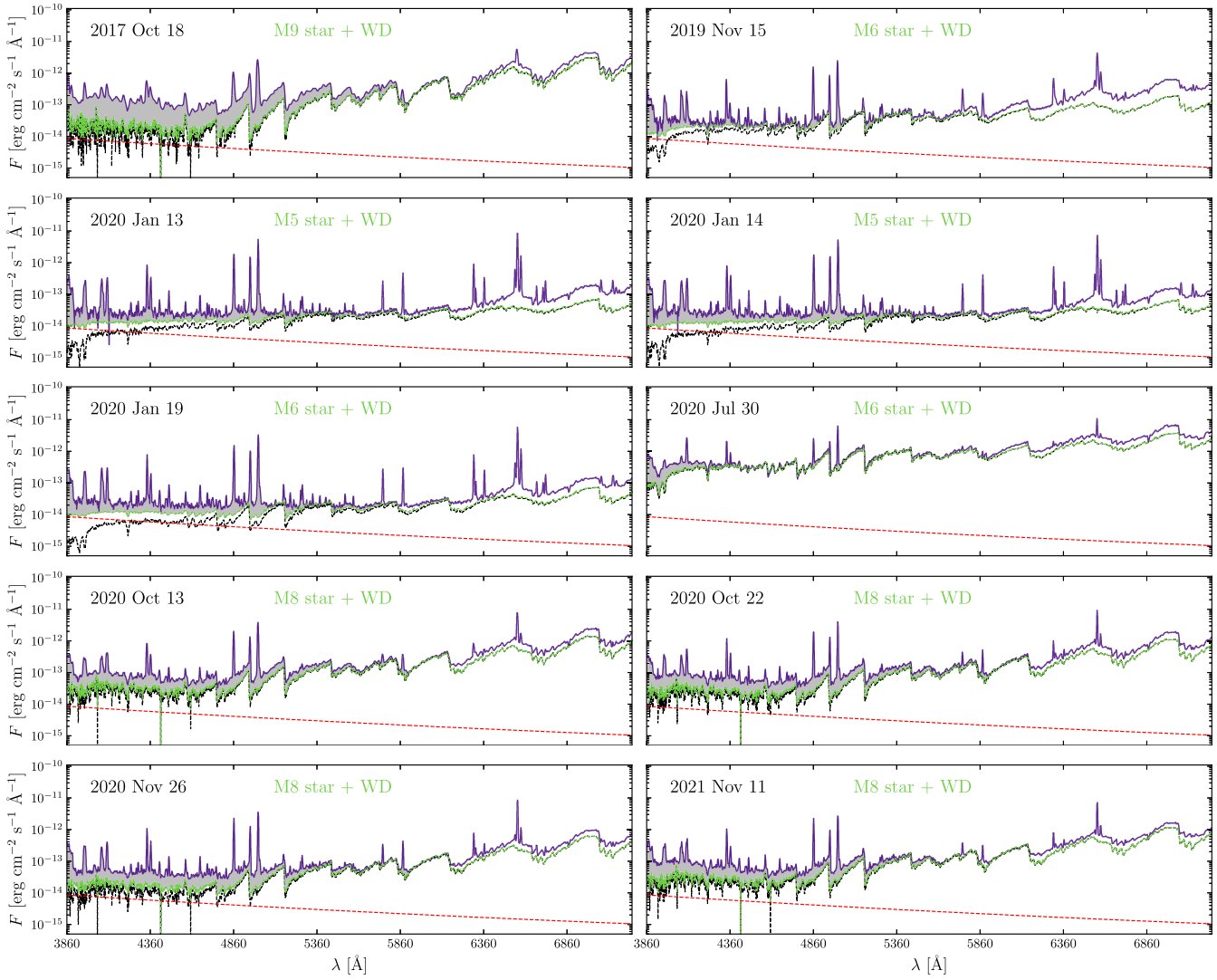

Figure A1. Extinction-corrected ARAS spectra of R Aqr from 2017 October 18 to 2021 November 11 (solid purple line). The spectra are compared with M-type star models from Fluks et al. (1994) (black dashed lines) and the contribution from the WD with the parameters estimated in Appendix B ($T_{\rm eff} = 40,000$ K and $L = 0.29$ L$_\odot$; red dashed line). A combined spectrum (M-type star + WD) is shown with a (green) dashed line. The grey shaded area represents the contribution of the accretion disc to the optical flux.

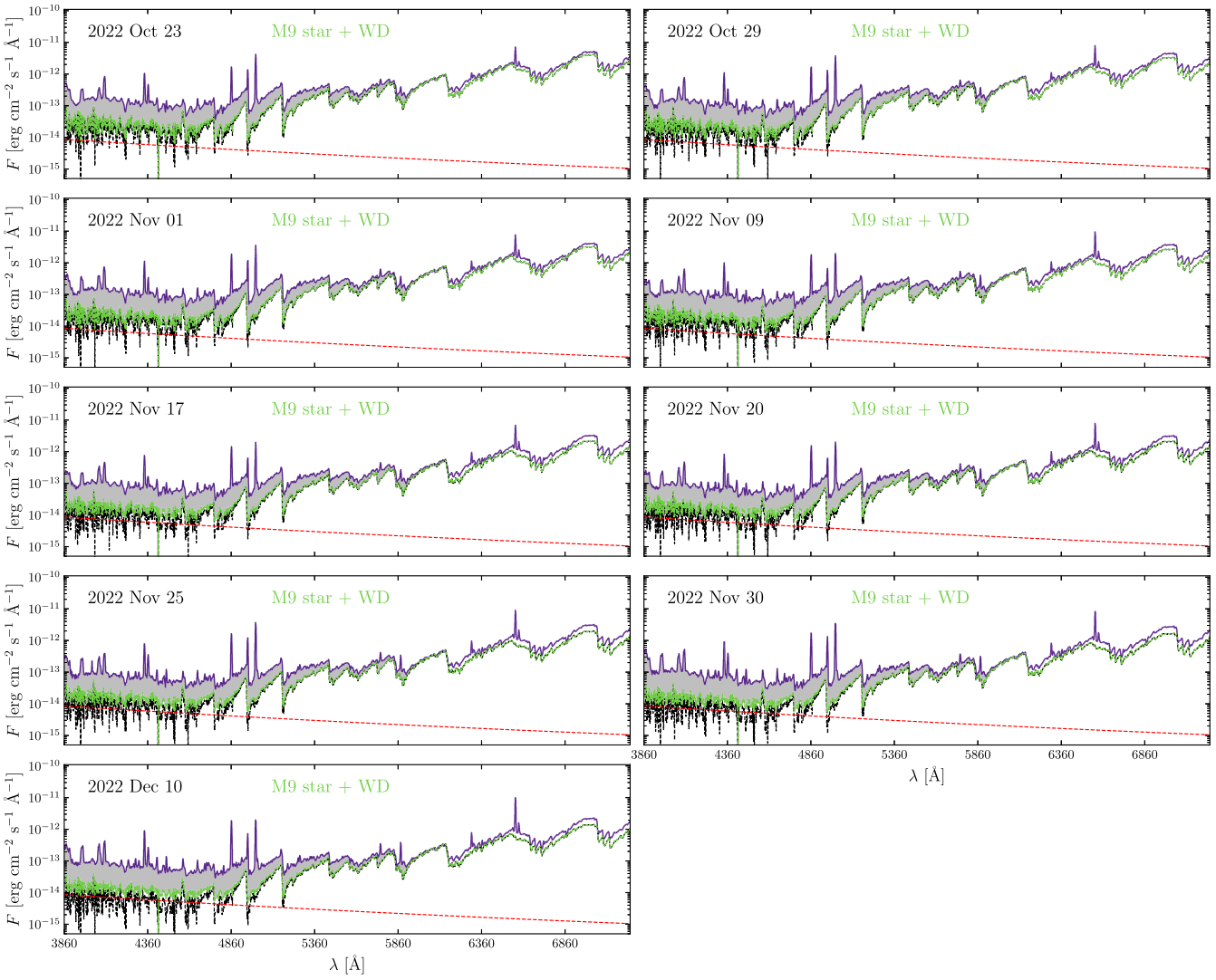

Figure A2. Same as Fig. A1 but for epochs between 2022 October 23 and 2022 December 10.

APPENDIX B: ULTRAVIOLET LUMINOSITY OF THE ACCRETION DISC

In this section, we present the analysis of UV data in order to estimate the contribution from the accretion disc to this wavelength. For this, we retrieved *IUE* spectra from R Aqr listed in the MAST with exposure times longer than 1000 s and corresponding to the low-dispersion and large aperture. These spectra cover the 1850–3350 Å wavelength range.

Fig. B1 presents a median spectrum obtained from combining all available near-UV *IUE* spectra. To correct for reddening, we used the extinction of the interstellar medium, $A_V = 0.1$ mag.

A blackbody spectrum was fitted to the dereddened median UV spectrum. This resulted in a model with a temperature of $T_{BB} = 25\,000$ K and a bolometric luminosity of $L_{WD} = 0.19^{+0.11}_{-0.04}$ L$_\odot$ at $d = 200^{+60}_{-20}$ pc. Using the Stefan–Boltzmann law, we estimated the WD's radius to be $R_{WD} = 0.025^{+0.008}_{-0.003}$ R$_\odot$. This model is compared in Fig. B1 with the near-UV median spectrum of R Aqr. An excess is unambiguously detected for $\lambda > 2910$ Å.

Finally, to estimate the contributing flux from the accretion disc to the UV band, we integrated the area between the median spectrum and the black body in the interval $2296 < \lambda_{UV} < 3350$ Å. After converting the integrated flux, the resulting luminosity is $L_{UV} = 0.07^{+0.04}_{-0.01}$ L$_\odot$.

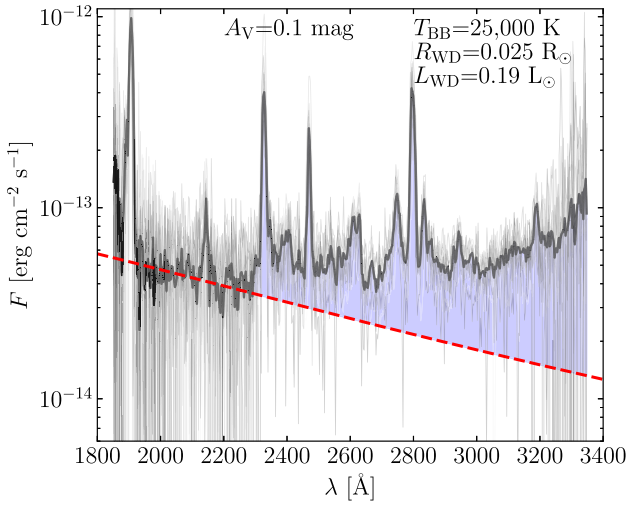

Figure B1. *IUE* spectrum of R Aqr (thick solid line) obtained by calculating the median of all available spectra in the MAST (thin lines). The dashed curve represents the contribution from a black body model with $T_{bb} = 25\,000$ K, $L_{WD} = 0.19\,L_\odot$, and $R = 0.025\,R_\odot$. The spectrum was corrected using an extinction of $A_V = 0.1$ mag. The shaded region represents the excess flux attributed to the contribution from the accretion disc.

APPENDIX C: A BONDI–HOYLE–LYTTLETON ACCRETION MODEL FOR R AQR

In this appendix, we construct a simple analytical model to investigate wind accretion in the R Aqr system. We assume the following orbital parameters are known:

$$M_1 = 1.0\,M_\odot, \tag{C1}$$

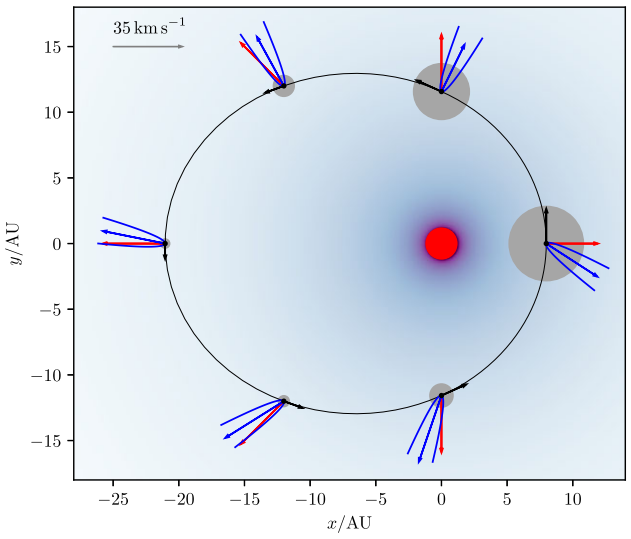

Figure C1. This schematic illustration depicts wind accretion on to a WD in a binary system, as viewed from the primary M-type star. Black points and arrows track the WD's position and orbital velocity. Red and blue arrows represent the local wind velocity and the relative velocity between the WD and the wind, respectively. The approximate shape of the bow shock at each position is indicated by blue parabolic curves. The size of the grey circle at each point corresponds to the relative mass accretion rate at that location. The colour gradient illustrates the density distribution of the wind of the primary M-type star.

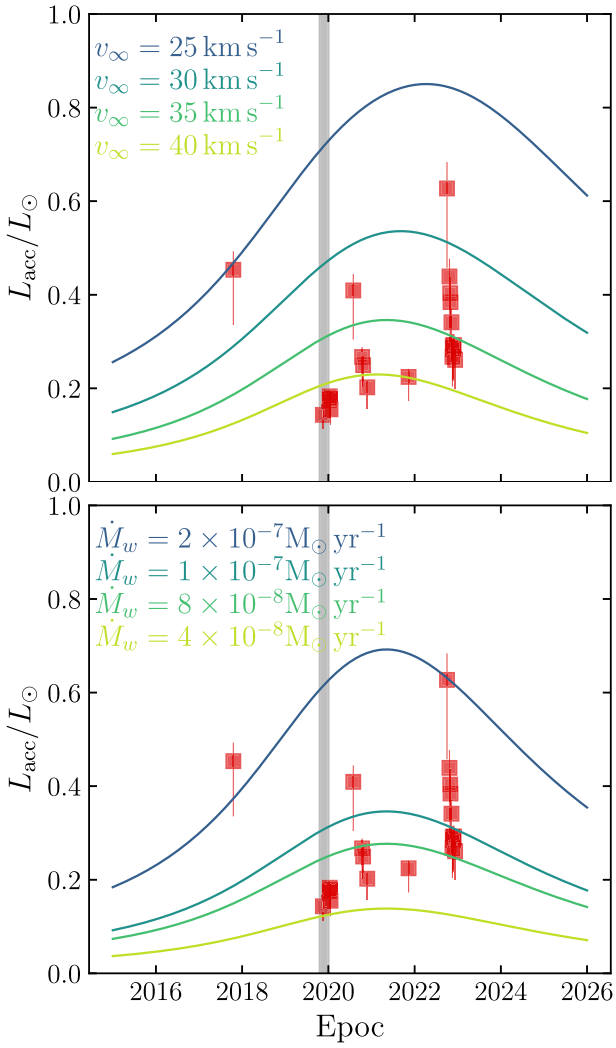

Figure C2. Model predictions for the accreiton luminosity. Top panel: four cases of v_∞ are considered for a mass-loss rate of $\dot{M}_{Mtype} = 10^{-7}$ M$_\odot$ yr^{-1} from the primary. Bottom panel: results are shown for $v_\infty = 35$ km s^{-1} and four different values of the mass loss rate $\dot{M}_{Mtype}$. In both panels, the squares represent the values (with errors) obtained from the ARAS spectra, allowing for a direct comparison between the analytic model and observations.

$$M_{WD} = 0.7\,M_\odot, \tag{C2}$$

$$e = 0.45, \tag{C3}$$

$$P = 42.4\,\text{yr}, \tag{C4}$$

where M_1 and M_{WD} represent the masses of the M-type primary and secondary WD star, e is the orbital eccentricity, and P is the orbital period. Applying Kepler's third law, we derive the semimajor axis $a = 14.51$ au. Fig. C1 provides a schematic representation of our wind accretion model.

Following a similar approach as in Theuns, Boffin & Jorissen (1996) and Saladino et al. (2018), we employ the Bondi–Hoyle–Lyttleton (BHL) model (Hoyle & Lyttleton 1939; Bondi & Hoyle 1944) to estimate the mass accretion rate on to the WD from the

primary's wind as

$$\dot{M}_{\rm BHL} = 4\pi \frac{(G M_{\rm WD})^2 \rho_w}{v_{\rm rel}^3}, \tag{C5}$$

where ρ_w is the wind density and $v_{\rm rel}$ represents the relative velocity between the WD and the wind.

The primary star's stellar wind is modelled using a typical β velocity law:

$$\boldsymbol{v}_w(r) = v_\infty \left(1 - \frac{R_1}{r}\right)^\beta \hat{r}, \tag{C6}$$

where $R_1 = 250\,{\rm R}_\odot \simeq 1.16$ au is the stellar radius, v_∞ is the terminal wind velocity, and r denotes the relative distance between the two stars. We adopt $\beta = 2$ which best reproduces the wind profile of cool stars (see Lamers & Cassinelli 1999).

Furthermore, assuming a constant mass loss rate $\dot{M}_{\rm Mtype}$, we apply the continuity equation to express the wind density as

$$\rho_w(r) = \frac{\dot{M}_{\rm Mtype}}{4\pi r^2 v_w} = \frac{\dot{M}_{\rm Mtype}}{4\pi a^2 v_\infty} \left(\frac{a}{r}\right)^2 \left(1 - \frac{R_1}{r}\right)^{-\beta}. \tag{C7}$$

While, for an elliptic trajectory

$$v_{\rm rel} = \sqrt{v_w^2 + v_{\rm WD}^2 - 2\, v_w v_{\rm WD}^r}, \tag{C8}$$

where

$$v_{\rm WD} = v_0 \sqrt{\frac{2a}{r} - 1}, \tag{C9}$$

$$v_{\rm WD}^r = v_0 \frac{e}{\sqrt{1-e^2}} \sin\varphi, \tag{C10}$$

and

$$v_0 = \sqrt{G(M_1 + M_{\rm WD})/a} \tag{C11}$$

is the mean orbital velocity of the WD.

As shown in more detail in Tejeda & Toalá (2024), equations (C5) and (C7) can be combined to calculate the mass accretion efficiency as

$$\eta = \frac{\dot{M}_{\rm acc}}{\dot{M}_{\rm Mtype}} = \frac{\dot{M}_{\rm BHL}}{\dot{M}_{\rm Mtype}} \left|\frac{v_w - v_{\rm WD}^r}{v_{\rm rel}}\right| = \left|1 - \frac{v_{\rm WD}^r}{v_w}\right| \left(\frac{M_{\rm WD}}{M_1 + M_{\rm WD}}\right)^2 \left(\frac{a}{r}\right)^2 \left(\frac{v_0}{v_{\rm rel}}\right)^4. \tag{C12}$$

This quantity represents the fraction of the primary's stellar wind captured by the WD star via BHL accretion. For the assumed orbital parameters of R Aqr, we find that, at pericentre ($\varphi = 0$) the mass accretion efficiency ranges from $\eta = 0.005$ to 0.02 for asymptotic wind velocities between 25 and 40 km s^{-1}, respectively.

Assuming that the captured material through wind accretion ultimately forms a standard thin accretion disc around the WD, we can estimate the expected disc luminosity as (Shakura & Sunyaev 1973)

$$L_{\rm acc} = \frac{1}{2} \frac{G M_{\rm WD}}{R_{\rm WD}} \dot{M}_{\rm acc} \simeq 0.44 \left(\frac{\eta}{0.01}\right) \left(\frac{\dot{M}_{\rm Mtype}}{10^{-7}\,{\rm M}_\odot\,{\rm yr}^{-1}}\right) \times \left(\frac{M_{\rm WD}}{0.7\,{\rm M}_\odot}\right) \left(\frac{R_{\rm WD}}{0.025\,{\rm R}_\odot}\right)^{-1} {\rm L}_\odot. \tag{C13}$$

Fig. C2 presents the predicted accretion luminosity for four different values of the terminal wind velocity (v_∞ = 25, 30, 35, and 45 km s^{-1}) and a fixed mass loss rate from the M-type star of $\dot{M}_{\rm Mtype} = 10^{-7}$ M$_\odot$ yr^{-1}. For comparison, the plot shows the results of the accretion luminosity estimated for the accretion disc in R Aqr.

The standard BHL model demonstrates broad agreement with the observational data, accurately predicting the order of magnitude of disc luminosity. This consistency is observed for the selected asymptotic wind velocities. Furthermore, for a given v_∞, the model aligns with observations when the mass loss rate varies between 4×10^{-8} and 2×10^{-7} M$_\odot$yr^{-1} (see bottom panel of Fig. C2).

The remaining discrepancies between the observations and our model can likely be attributed to the inherent simplicity of the later and the assumption of a smooth β law for the stellar wind. In reality, the wind environment of M-type stars is expected to be more variable and/or inhomogeneous and pulsations are likely to cause abrupt variations in local wind properties.

This paper has been typeset from a TEX/LATEX file prepared by the author.